

Mapping eccentricity evolutions between numerical relativity and effective-one-body gravitational waveforms

Alice Bonino ^{1,*} Patricia Schmidt ^{1,†} and Geraint Pratten ^{1,‡}

¹*School of Physics and Astronomy and Institute for Gravitational Wave Astronomy,
University of Birmingham, Edgbaston, Birmingham, B15 2TT, United Kingdom*

(Dated: November 5, 2024)

Orbital eccentricity in compact binaries is considered to be a key tracer of their astrophysical origin, and can be inferred from gravitational-wave observations due to its imprint on the emitted signal. For a robust measurement, accurate waveform models are needed. However, ambiguities in the definition of eccentricity can obfuscate the physical meaning and result in seemingly discrepant measurements. In this work we present a suite of 28 new numerical relativity simulations of eccentric, aligned-spin binary black holes with mass ratios between 1 and 6 and initial post-Newtonian eccentricities between 0.05 and 0.3. We then develop a robust pipeline for measuring the eccentricity evolution as a function of frequency from gravitational-wave observables that is applicable even to signals that span at least $\gtrsim 7$ orbits. We assess the reliability of our procedure and quantify its robustness under different assumptions on the data. Using the eccentricity measured at the first apastron, we initialise effective-one-body waveforms and quantify how the precision in the eccentricity measurement, and therefore the choice of the initial conditions, impacts the agreement with the numerical data. We find that even small deviations in the initial eccentricity can lead to non-negligible differences in the phase and amplitude of the waveforms. However, we demonstrate that we can reliably map the eccentricities between the simulation data and analytic models, which is crucial for robustly building eccentric hybrid waveforms, and to improve the accuracy of eccentric waveform models in the strong-field regime.

I. INTRODUCTION

Gravitational-wave (GW) observations are poised to become an instrumental tool in constraining the formation and evolutionary pathways of stellar mass black holes. To date, a wide range of evolutionary mechanisms have been proposed, see [1–4] for recent reviews, and it is crucial that we develop the tools to robustly distinguish between the mechanism. Identifying the dominant mechanisms, and understanding their respective branching ratios, is expected to yield significant insight into stellar physics, binary interactions, and relativistic astrophysics [5–8]. Unfortunately, the predicted mass distribution of stellar mass black hole can be highly degenerate between the many different formation channels, so we must appeal to other observables to help distinguish between the channels. The spin of the black holes and the eccentricity of their orbits will leave characteristic imprints in the emitted gravitational-wave signal, making them powerful tracers of the underlying formation channel.

Binaries that form through isolated evolution [9–14] are typically expected to circularize through the emission of gravitational radiation [15, 16]. This process is particularly efficient, such that these binaries will appear quasi-circular by the time they enter the sensitivity band of the current generation of ground-based detectors. However, binaries that are formed through recent dynamical

interactions are expected to have non-negligible eccentricities [17–21]. This is particularly expected for dense stellar environments, such as globular clusters and active galactic nuclei, where the rate of dynamical interactions and captures can be enhanced. A robust measurement of eccentricity is therefore thought to be a particularly clean tracer for such dynamical interactions [22]. Spin misalignment [23–25] is also thought to be characteristic signature for such dynamically formed binaries, though this may again be degenerate with other formation channels [26–28].

A current limitation to extracting information on eccentricity from the current generation of ground-based GW detectors is the lack of sensitivity below 20 Hz. Recent studies suggest that eccentricities ≥ 0.05 at a gravitational-wave frequency of 10 Hz will be necessary to extract eccentric information based on the current generation of detectors at design sensitivity [29]. Improving the low-frequency sensitivity of the next-generation of ground-based detectors, including Cosmic Explorer [30] and the Einstein Telescope [31], could lead to significant improvements and allow us to resolve eccentricities down to the $\sim 10^{-3}$ level, e.g. [32, 33].

Similarly, multiband observations between space-based and ground-based detectors may be a potential route to extracting the natal eccentricities of stellar mass black holes [34–36], though the event rates are highly uncertain [37, 38] and they require a robust framework for tracking and modelling the evolution of eccentricity over a period of year(s).

In recent years, significant effort has been invested in incorporating eccentricity into the current generation of waveform models. Within the post-Newtonian (PN) ap-

* axb1612@student.bham.ac.uk

† P.Schmidt@bham.ac.uk

‡ G.Pratten@bham.ac.uk

proximation [39], which assumes weak-fields and small velocities [$\epsilon \sim GM/(c^2 r) \sim (v/c)^2 \ll 1$], the conservative dynamics for generic orbits are known up to 5PN [40–50] and radiative effects up to 3PN [51–59]. This has led to the construction of numerous eccentric waveform approximants within the PN framework, e.g. [60–65]. Likewise, there have been numerous developments within the gravitational self-force (GSF) and scattering paradigms, e.g. [66–72]. However, whilst these provide an accurate description of the gravitational-wave signals throughout the inspiral, they are only valid up to moderate eccentricities ($e \sim 0.1$) and are not reliable as the binary approaches merger.

To mitigate against such limitations, one can appeal to numerical relativity (NR) simulations to help model the complete inspiral-merger-ringdown (IMR) signal from eccentric binaries [73–78]. Such catalogs have enabled the construction of eccentric NR surrogates [79, 80] as well as PN-NR hybrids that blend analytical information from PN evolutions with the NR simulations [65, 73, 81–83]. Even though NR simulations cover a comparatively restricted region of the parameter space, they do provide the full non-linear solutions of the Einstein field equations and play a crucial role in accurately modelling the remnant black hole and providing an accurate representation of the GW signal through merger. As such, whilst eccentric NR surrogates and hybrid models are highly accurate, they are necessarily constrained by the poor parameter space coverage, accuracy, and finite length of available NR simulations, which often do not capture the early inspiral regime.

One alternative approach is the so called effective-one-body (EOB) framework [84–87], which is a successful paradigm for modelling the complete GW signal emitted by compact binaries on arbitrarily eccentric orbits. Some of the first studies on incorporating eccentricity into the EOB framework were outlined in [88–90]. There have been numerous subsequent technical developments that have dramatically improved the accuracy of eccentric EOB models [91–102]. Of the available models, SEOBNRv4EHM, [98] `TEOBResumS-Da11` [92–94, 103–105], and SEOBNRE [90] are the most mature. An extension of SEOBNRE to eccentric binaries with precessing spins has recently been presented [106].

However, a key limitation in comparing eccentric waveform models is that eccentricity itself is not gauge invariant in general relativity. This means that we need to exercise due caution if we are to ensure that we are comparing equivalent binary configurations. A number of different estimators for eccentricity have been introduced with [75] having recently identified an estimator that can be applied directly to the GW signal and has the correct Newtonian limit. If we are able to construct a map between models that allows us to set up self-consistent initial conditions (ICs), we can start to meaningfully compare the physics content of each model and the subsequent evolution of the eccentricity. This also has implications for understanding astrophysical forma-

tion scenarios, in which recent work has highlighted the need for self-consistent definitions of eccentricity between gravitational-wave data analysis and astrophysical population simulations [107].

The aim of this work is to (i) extend the parameter space coverage in available catalogs of NR simulations for eccentric binary black holes; (ii) to build a robust pipeline for measuring the eccentricity evolution from numerical relativity waveforms that is applicable even for short-duration signals; and (iii) to identify a map between the measured eccentricity evolution and initial conditions. We revisit the framework introduced in [108] and demonstrate its robustness against our suite of new aligned-spin eccentric NR simulations and `TEOBResumS-Da11`.

The paper is organised as follows. Section II provides an extensive overview of the new suite of NR simulations we have performed. Section III furnishes the methodology we use to measure the eccentricity from the numerical data and assesses the impact of numerical errors on the procedure. Section IV provides a detailed description and assessment of the mapping between initial conditions from numerical simulations and one particular EOB waveform model, `TEOBResumS-Da11`. In Sec. V we discuss and summarize the main results of this work. Throughout the paper, we use $G = c = 1$ unless otherwise stated.

II. NUMERICAL SIMULATIONS

A. Overview

In this paper, we present a catalog of 28 eccentric NR simulations performed with the open-source Einstein Toolkit [109, 110] within the moving punctures framework [111, 112]. We use conformally flat Bowen-York initial data [113, 114] as computed using the `TwoPunctures` thorn [115]. Evolution is performed using the W -variant [116] of the Baumgarte-Shapiro-Shibata-Nakamura (BSSN) formulation of the Einstein field equations [117, 118] as implemented by the `McLachlan` thorn. The black holes are evolved using the moving punctures gauge conditions [111, 112]. The lapse is evolved using a 1+log slicing condition [119] and the shift is evolved using the hyperbolic $\tilde{\Gamma}$ -driver equation [120]. Spatial derivatives are computed using an 8th order accurate finite differencing scheme together with Kreiss-Oliger dissipation [121]. The apparent horizons (AH) are computed using the `AHfinderDirect` [122]. The black hole spins are estimated through a dynamical horizon formalism as implemented in `QuasiLocalMeasures` where [123–125]

$$S = \frac{1}{8\pi} \oint_{\text{AH}} n^a \varphi^b K_{ab} d^2A, \quad (1)$$

where φ^a denotes an (approximate) axial Killing vector field, n^a a spacelike unit normal to the horizon, and K_{ab} the extrinsic curvature. Adaptive mesh refinement

is provided by `Carpot` [126], with the near-zone being covered by high-resolution Cartesian grids. The wave extraction zone is computed using the `Llama` infrastructure [127, 128], whose grids are adapted to the spherical topology of the zone and allow for high-resolution extraction out to comparatively large radii relative to standard Cartesian grids. Gravitational waves are extracted from the simulations using the Newman-Penrose Weyl scalar Ψ_4 , as provided by the `WeylSca14` thorn [129]. As is conventional, Ψ_4 is decomposed into spin-weighted spherical harmonics of spin weight $s = -2$, such that

$$r\Psi_{4,\ell m} = \int_0^{2\pi} \int_0^\pi -{}^2Y_{\ell m}^*(\theta, \phi)\Psi_4(\theta, \phi) \sin\theta d\theta d\phi, \quad (2)$$

where ${}^2Y_{\ell m}^*$ denotes the complex conjugate of the spin-weighted spherical harmonics and (θ, ϕ) the spherical coordinates on the unit sphere. The gravitational-wave strain h can then be derived from $\Psi_4 \equiv -\ddot{h}$ through fixed frequency integration (FFI) [130].

To help mitigate against near-field gauge effects, we calculate the asymptotic waveform at future null infinity \mathcal{I}^+ using extrapolation, e.g. [131, 132]. In this framework, we extract a quantity \mathcal{Q} on a series of spheres of increasing radii and perform a least-squares fit to find the asymptotic behaviour of the non-oscillatory function \mathcal{Q}

$$\mathcal{Q}(u_i, r) = \sum_{n=0}^N \frac{\mathcal{Q}_n}{r^n}, \quad (3)$$

such that the leading order coefficient \mathcal{Q}_0 represents the asymptotic value at \mathcal{I}^+ at an order N . For a subset of simulations, we also use the perturbative framework introduced in [133] to extrapolate $r\Psi_4$, finding good agreement between the two methods.

B. Eccentric Initial Conditions

In order to produce eccentric initial data, we use a PN approximation to estimate the momenta of the black holes given a specific eccentricity at some reference separation. We follow the approach outlined in [134] in which the tangential momentum is perturbed away from the quasi-circular value by a correction factor that is derived within a quasi-Keplerian parametrization [54]. This procedure was used in [134] to iteratively construct low-eccentricity initial data, and in [73] to construct initial data with a prescribed eccentricity. As detailed in [73, 134], the correction factor for the tangential momenta λ_t in the low eccentricity limit is given by

$$\lambda_t(D, e_0, \nu, \text{sign}) = 1 + \frac{e_0}{2} \times \text{sign} \times \left[1 - \frac{1}{D}(\nu + 2) \right], \quad (4)$$

where $\nu = m_1 m_2 / M^2$ is the symmetric mass ratio, $M = m_1 + m_2$ the total mass, D the initial orbital separation, e_0 is the initial eccentricity, and $\text{sign} = \pm 1$ depends

on the initial phase. However, as discussed in [73], the correction factor that we apply to the tangential momentum is taken to be the average between the inverse of λ_t with a plus sign plus and λ_t with a minus sign, i.e.

$$\bar{\lambda}_t^0(D, e_0, \nu) = \frac{1}{2} \left[\lambda_t(D, e_0, \nu, +1)^{-1} + \lambda_t(D, e_0, \nu, -1) \right]. \quad (5)$$

C. Catalog of Simulations

The suite of eccentric aligned-spin NR simulations presented here spans a range of parameters. The mass ratio $q = m_1/m_2 \geq 1$ of the binaries' components ranges from $q = 1$ to $q = 6$ with initial eccentricities e_0 up to moderate values of 0.3. The largest dimensionless black hole spin that we consider for the i -th black hole is $|\chi_i| \simeq 0.5$. The simulations cover between 3 and 15 complete orbits before merger, depending on the binary parameters, typically starting at an initial separation of $D \sim 12.5M$.

The Cartesian grids are implemented using the `Carpot` thorn, which provides a multiblock scheme that implements Berger-Oliger adaptive mesh refinement. The grids are nested, such that there are L^k levels of increasing resolution, i.e., $\Delta x^k = \Delta x^{k-1}/2$. The innermost Cartesian grids are initialized such that their radii are $\sim 1.2r_{\text{AH}}$, where r_{AH} is the radius of the coordinate apparent horizon. Likewise, the outermost Cartesian grid, L^0 , spans a domain that covers both black holes with a resolution set by the transition to the spherical grids managed by the `Llama` thorn. The resolution of the radial grids when extracting the gravitational waves is guided by the expected wavelength of higher multipole moments in the ringdown, typically resulting in a resolution $\Delta x < 1.0M$.

In Tab. I, we provide a summary of the simulation properties for the catalog presented here, including the number of complete GW cycles up to merger N_{cycles} computed from Ψ_4 , where we define the merger time as the time of the maximum rms amplitude of the $(\ell, m) = (2, \pm 2)$ modes and remove all data before junk radiation plus $50M$ when computing the number of GW cycles. We also give the Christodoulou mass of the remnant black hole, M_f as well as its dimensionless spin $\chi_f = S_f/M_f^2$, with the Christodoulou mass given by [135]

$$M_f = \sqrt{M_{\text{irr}}^2 + \frac{S_f^2}{4M_{\text{irr}}^2}}, \quad M_{\text{irr}} = \sqrt{\frac{A}{16\pi}}, \quad (6)$$

where M_{irr} is the irreducible mass and is related to the area A of the BH horizon. The last column in Tab. I is the angular frequency measured at the first periastron $M\omega_p^0$, see Sec. III for further details. The $\{q, \chi_{\text{eff}}, e_0\}$ parameter space covered by our simulations is shown in Fig. 1.

In addition to the final mass and spin of the remnant, we also compute the Christodoulou mass and spin associated with each black hole horizon after equilibrium

is reached at a simulation time of $t = 100M$. This allows us to evaluate the remnant spin fit of Ref. [136] for quasi-circular non-precessing BBHs and compare it to our measurements. We find that for all our simulations the absolute difference between the quasi-circular prediction and our eccentric mergers is on the order of $\mathcal{O}(10^{-3})$, consistent with previous findings for equal-mass, moderately eccentric systems [79].

We also compute the peak luminosity taking into account all multipoles of Ψ_4 up to $\ell = 6$ [137]

$$\mathcal{L}_{\text{peak}} = \max_t \frac{1}{16\pi} \sum_{\ell=2}^6 \sum_{m=-\ell}^{\ell} |\dot{h}_{\ell m}^{\infty}(t)|^2, \quad (7)$$

where $h_{\ell m}^{\infty}$ denotes the strain modes obtained via FFI and extrapolated to infinity. We note that we exclude the ($m = 0$)–modes from our calculation. The obtained peak luminosity for each simulation is given in the final column of Tab. I. Comparing to the fit for quasi-circular simulations from Ref. [138], we find small differences of the order of 10^{-3} , suggesting that the binaries have circularised sufficiently before the peak emission is reached.

Finally, we compute the fractional periastron advance per orbit following Eq. (29) of [139]

$$\frac{\Omega_{\text{orb}}^p}{\Omega_r^p} = \frac{\phi_{\text{orb}}(t_{i+1}^p) - \phi_{\text{orb}}(t_i^p)}{2\pi}, \quad (8)$$

where t_i^p and t_{i+1}^p indicate two consecutive periastra passages, Ω_{orb}^p and Ω_r^p are respectively the orbital and the radial frequencies at periastron passages, and ϕ_{orb} is the orbital phase of the binary. We define the periastron advance per orbit as

$$K \equiv \frac{\Omega_{\text{orb}}^p}{\Omega_r^p} - 1. \quad (9)$$

Figure 2 shows the periastron advance for all simulations that have at least 16 complete GW cycles. The periastron precession K across all simulations spans $\sim 0.2 - 0.63$, in agreement with Fig. (7) of [139].

III. ECCENTRICITY ESTIMATION

A. Introduction

As has been extensively discussed in the literature, e.g. see [140–143], eccentricity is not a uniquely defined quantity in general relativity and gauge ambiguities make comparisons between measurements difficult. A number of estimators have been proposed in the literature, including a more recent definition of eccentricity that resolves some of these gauge ambiguities [73]. We are particularly interested in inferring the evolution of the eccentricity directly from the gravitational-wave signal, be it on real data, (semi-)analytical waveform models, or numerical relativity simulations. This requires a number

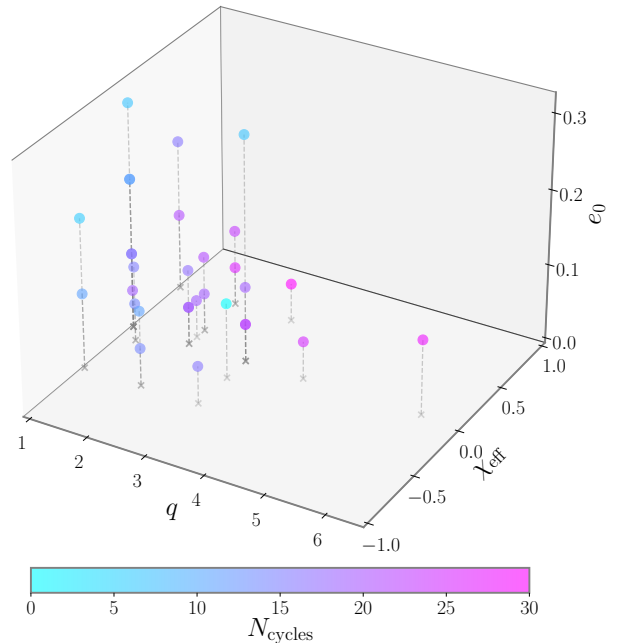


FIG. 1. Parameter space coverage of our NR simulations listed in Tab I. We show the mass ratio q , the effective aligned-spin χ_{eff} , and the initial PN eccentricity e_0 . The colour represents the number of complete GW cycles.

of key ingredients: i) a robust estimator for the eccentricity, ii) a parameter that describes the position of the compact objects on the orbit, iii) a parameter that characterizes the size of the orbit, and iv) a mapping between the time and some appropriately averaged frequency. In tackling this challenge, two highly complementary approaches have recently been presented in [108] and [143]. The framework outlined in [143] provides a very thorough and detailed discussion on the challenges of inferring eccentricity and the robustness of the implementation. To fully characterize an eccentric orbit, [143] adopts the eccentricity estimator introduced in [75] $e_{\text{gw}}(t)$ together with a generalization of the Newtonian mean anomaly $l_{\text{gw}}(t)$ over an interval between two consecutive periastron passages t_i^p and t_{i+1}^p defined as

$$l_{\text{gw}}(t) = 2\pi \frac{t - t_i^p}{t_{i+1}^p - t_i^p}. \quad (10)$$

In order to estimate the reference frequency, [143] uses an orbit-averaged frequency $\hat{\omega}_{22}$ that is again defined between two consecutive periastron passages [75, 144]. The framework presented in [108] also adopts the eccentricity estimator defined in [75] but uses the value of the eccentricity at an initial frequency such that the system always starts at the apastron. In this instance, the joint specification of the initial eccentricity and initial frequency replaces the eccentricity and mean anomaly. The final ingredient introduced in [108] is to use the mean of the fre-

ID	q	$\chi_{1,z}$	$\chi_{2,z}$	χ_{eff}	e_0	$D [M]$	N_{cycles}	M_f	χ_f	$M\omega_{22}^p$	$\mathcal{L}_{\text{peak}}$
0001	1	0	0	0	0.05	12.5	19	0.9515	0.6861	0.052	0.00105
0002	1	0	0	0	0.1	12.5	16	0.9513	0.6864	0.062	0.00106
0003	1	0.5	-0.5	0	0.1	12.5	16	0.9511	0.6855	0.060	0.00107
0004	1	-0.5	-0.5	-0.5	0.1	12.5	11	0.9620	0.5261	0.068	0.00086
0005	1	0.5	0.5	0.5	0.1	12.5	21	0.9327	0.8312	0.058	0.00137
0006	1	0	0	0	0.2	12.5	11	0.9516	0.6839	0.080	0.00103
0007	1	0.5	-0.5	0	0.2	12.5	11	0.9514	0.6830	0.070	0.00104
0008	1	-0.5	-0.5	-0.5	0.2	12.5	6	0.9622	0.5323	0.060	0.00090
0009	1	0.5	0.5	0.5	0.2	12.5	16	0.9330	0.8299	0.060	0.00135
0010	1	0	0	0	0.3	12.5	7	-	-	0.060	0.00109
0011	1.24	0.31	-0.46	-0.1163	0.05	11.05	14	0.9527	0.6869	0.060	0.00102
0012	1.24	0.31	-0.46	-0.1163	0.1	11.05	15	0.9524	0.6879	0.062	0.00104
0013	2	0	0	0	0.05	12.5	20	0.9613	0.6236	0.050	0.00080
0014	2	0	0	0	0.05	12.1579	18	0.9611	0.6235	0.054	0.00080
0015	2	-0.5	-0.5	-0.5	0.05	12.5	14	0.9700	0.4273	0.054	0.00064
0016	2	0.5	0.5	0.5	0.05	12.5	26	0.9448	0.8045	0.050	0.00107
0017	2	0	0	0	0.1	12.5	17	0.9614	0.6226	0.060	0.00079
0018	2	-0.5	-0.5	-0.5	0.1	12.5	11	0.9699	0.4264	0.068	0.00064
0019	2	0.5	0.5	0.5	0.1	12.5	23	0.9445	0.8048	0.060	0.00108
0020	3	0	0	0	0.05	12.5	22	0.9713	0.5402	0.052	0.00054
0021	3	0	0	0	0.05	12.379	22	0.9712	0.5399	0.052	0.00054
0022	3	-0.5	-0.5	-0.5	0.05	12.379	16	0.9780	0.2991	0.054	0.00043
0023	3	0.5	0.5	0.5	0.05	12.379	30	0.9582	0.7685	0.050	-
0024	3	0	0	0	0.1	12.5	19	-	-	0.062	0.00054
0025	3	0.1	-0.3	-0.2	0.1	12.5	19	0.9703	0.5747	0.064	0.00056
0026	3	0	0	0	0.3	12.5	7	-	-	0.100	0.00056
0027	4	0	0	0	0.05	12.379	25	0.9778	0.4715	0.052	0.00038
0028	6	0	0	0	0.1	12.83	28	0.9854	0.3727	0.060	0.00022

TABLE I. Summary of the eccentric NR simulations presented in this work. The first column gives the identifier of the simulation. The following columns indicate the mass ratio q , the z -components of the dimensionless spins $\chi_{1,z}$ and $\chi_{2,z}$, the effective spin χ_{eff} , the initial PN eccentricity e_0 , the initial separation D/M , the number of complete GW cycles up to the rms peak of the $(2, \pm 2)$ -modes N_{cycles} as well as the mass M_f and spin χ_f of the final black hole, the angular frequency at the first periastron $M\omega_{22}^p$ measured from the $(2, 2)$ -mode of Ψ_4 and the peak luminosity.

quencies between the periastra $\omega_{22}^p(t)$ and apastras $\omega_{22}^a(t)$ to estimate a monotonically increasing mean frequency $\bar{\omega}(t)$. Here we build on the methodology introduced in [108]. We note that the choice of using the mean frequency $\bar{\omega}(t)$ rather than $\hat{\omega}_{22}$ is motivated by the comparison of our numerical simulations against the EOB model `TEOBResumS-Dalí` in Sec. IV. However, the framework that will be presented below can also be applied to $\hat{\omega}_{22}$.

B. Methodology

The starting point for our discussion is the choice of the eccentricity estimator. Whilst this issue has previously been outlined in the literature, e.g. [73, 75, 93, 108, 140, 142, 143, 145–147], we include some discussion here for completeness. In the Newtonian limit, the eccentricity is uniquely defined by the separation of the binary at its periastron r^p and apastron r^a

$$e_{\text{Newt.}}(t) = \frac{r^a - r^p}{r^a + r^p}. \quad (11)$$

However, the Newtonian expression rapidly breaks down as PN corrections are included with additional parameters being required to fully characterize the eccentricity. Moreover, an eccentricity defined through the trajectories of the binary is gauge dependent, see [75, 139, 143, 148]. The second key drawback is that the estimator defined in Eq. (11) depends on quantities that are not directly observable through GWs, which impedes the applicability of the estimator to GW observations.

To mitigate against some of these issues, an estimator defined from the *orbital* frequencies at the periastron Ω_{orb}^p and apastron passages Ω_{orb}^a was introduced in [140] and is given by

$$e_{\Omega_{\text{orb}}}(t) = \frac{\sqrt{\Omega_{\text{orb}}^p(t)} - \sqrt{\Omega_{\text{orb}}^a(t)}}{\sqrt{\Omega_{\text{orb}}^p(t)} + \sqrt{\Omega_{\text{orb}}^a(t)}}. \quad (12)$$

This estimator has the correct Newtonian limit Eq. (11) but is also estimated from orbital trajectories, leading to the same caveats as before. An estimator based on the GW frequency of the $(2, 2)$ -mode, $\omega_{22} = d\phi_{22}/dt$, was

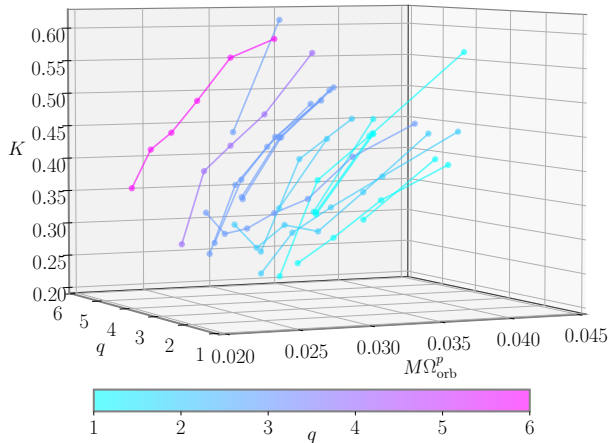


FIG. 2. Periastron advance per orbit K as a function of orbital frequency at periastra passages (marked by the dots) for our NR simulations that span at least 16 complete GW cycles, coloured by mass ratio q .

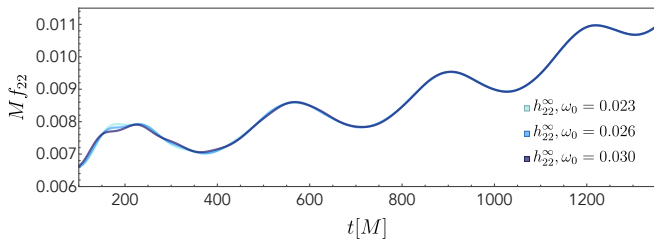


FIG. 3. Gravitational-wave frequency $f_{22} = \omega_{22}/(2\pi)$ obtained from h_{22}^{∞} using different values of ω_0 for the simulation with ID:0001. Depending on the choice of ω_0 that is used to carry out the FFI, the location of the first peak varies.

introduced in Ref. [149] and is given by

$$e_{\omega_{22}}(t) = \frac{\sqrt{\omega_{22}^p(t)} - \sqrt{\omega_{22}^a(t)}}{\sqrt{\omega_{22}^p(t)} + \sqrt{\omega_{22}^a(t)}}. \quad (13)$$

This estimator has the joint benefit of being gauge-independent and directly observable from the GW signal alone. However, it was noted in [75] that Eq. (13) does not obey the Newtonian limit, see also the discussion in [143]. To correct for this, [75] proposed a modified estimator defined by

$$e_{\text{gw}}(t) = \cos\left(\frac{\Psi(t)}{3}\right) - \sqrt{3} \sin\left(\frac{\Psi(t)}{3}\right), \quad (14)$$

where

$$\Psi(t) = \arctan\left(\frac{1 - e_{\omega_{22}}^2(t)}{2e_{\omega_{22}}(t)}\right). \quad (15)$$

Unless otherwise stated, we will adopt the eccentricity estimator $e_{\text{gw}}(t)$ given in Eq. (14) for the remainder of this work.

In order to measure the eccentricity from the NR data, we first need to determine $\omega_{22}(t)$. For each simulation in Tab. I, we follow the steps described in Sec. II to obtain the extrapolated multipole moments $\Psi_{4,\ell m}$, from which we calculate the extrapolated strain modes $h_{\ell m}^{\infty}$. This requires us to choose a physically motivated low-frequency cutoff ω_0 for the FFI that suppresses spurious non-linear drifts arising from the numerical integration and the amplification of unphysical frequencies resulting from spectral leakage [130]. The choice of ω_0 can impact the location of the first peak in the GW frequency, which in turn will impact the measured eccentricity (see App. A). An example of this is shown in Fig. 3 for three different values of ω_0 . As a consistency check on the above procedure, we compare against the strain h that is directly calculated from the metric perturbations via the Regge-Wheeler-Zerilli equations [150–152], as provided in the SXS waveform catalog [153]. Using SXS:BBH:1360, we find good agreement between the two methods for estimating h , with small variations in ω_0 having a subdominant impact on the h inferred using the FFI (see App. A). For our analyses, we choose $\omega_0 = \omega_{22}^p/2$, where ω_{22}^p is the frequency of $\Psi_{4,22}$ at the time of the first periastron.

After performing the time integration, we remove the junk radiation in all the simulations being mindful of preserving the first peak of $\omega_{22}(t)$. We have checked that this procedure is robust across all of our simulations and adopt $t_{\text{min}} \equiv 100M$.

Next we need an algorithm to identify the peaks in the GW frequency, which correspond to the periastron and apastron passages. Rather than fitting the first and second derivatives to identify the peaks, as was done in [108], we instead opt to use a rational function to calculate the residual between the frequency and its secular trend. We find this to be more robust than using derivatives due to the presence of numerical noise. After isolating the peaks, we fit the maxima and the minima of the frequency using a linear fit if only two peaks are available and a nonlinear rational fit of the form $(a + bx)/(1 + cx)$ when more peaks are available. We typically find rational functions to be more robust than an equivalent high-order polynomial. In order for the procedure to work, we require at least two peaks to be present, though we caution against the accuracy of the estimated eccentricity in this limit, see the discussion below in Sec. III C 1.

As discussed in [108], it is convenient to define the eccentricity as a function of a monotonically increasing frequency, providing a bijective correspondence between the eccentricity and the frequency. There are two possible choices for defining such a frequency that have been

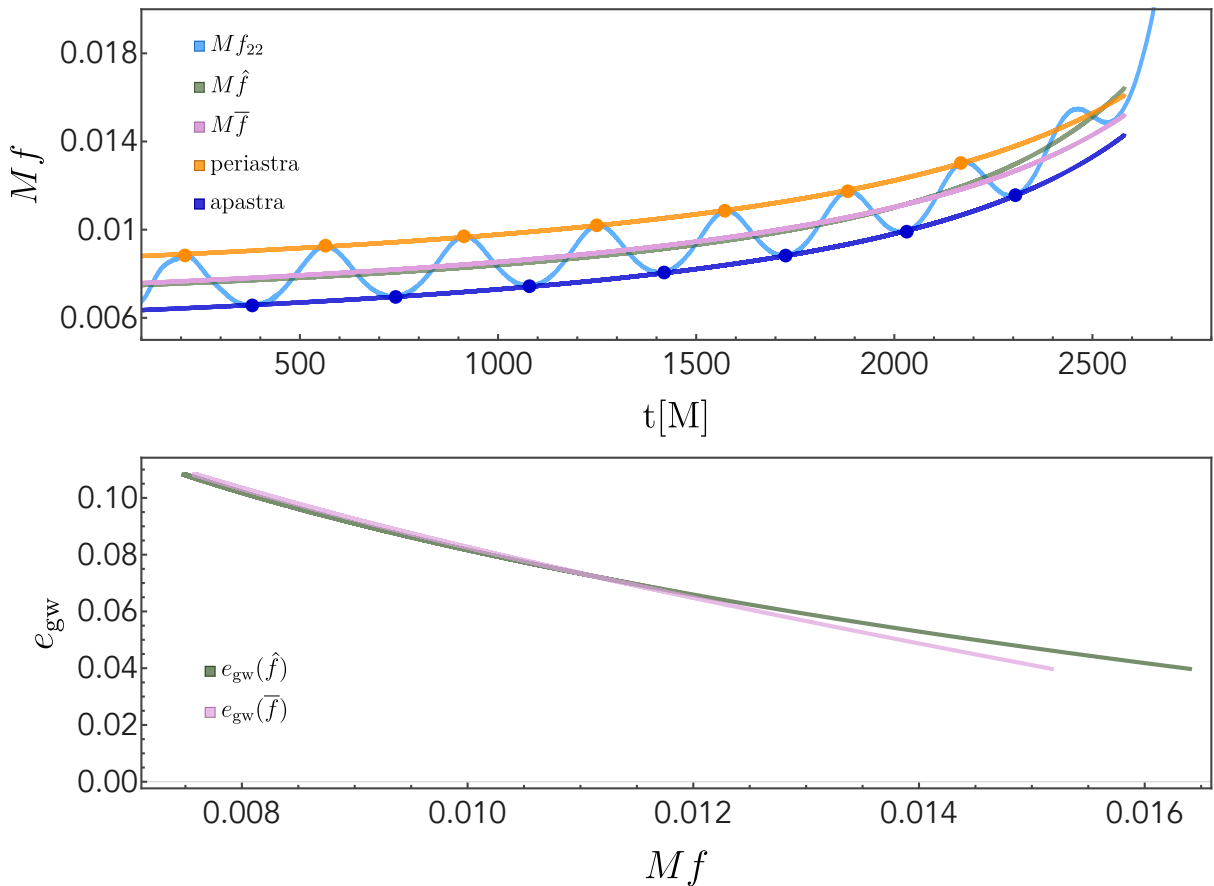


FIG. 4. Illustration of the end-to-end procedure to measure the eccentricity from a GW signal for our $q = 6$ simulation (ID:0028). The top panel shows the GW frequency (light blue), the fits of the apastron (orange) and periastron (blue) following the procedure described in the main text. We also show the two monotonic frequencies \bar{f} (pink) and \hat{f} (green). The bottom panel shows the measured evolution of the eccentricity as a function of either \hat{f} (green) or \bar{f} (pink).

adopted in the literature: The first is to define a *mean* GW frequency from the (2, 2)-mode [108], as

$$\bar{f} \equiv \frac{1}{2} (f_{22}^p + f_{22}^a), \quad (16)$$

where $f_{22}^X = \omega_{22}^X / (2\pi)$ and X denotes the periastron (p) or apastron (a) respectively.

The second choice is to introduce an *average* GW frequency \hat{f} that provides an orbit average between any two consecutive periastra or apastron [75, 143] enumerated by the index i

$$\begin{aligned} \hat{f}_{22,i}^X(t) &= \frac{1}{t_{i+1}^X - t_i^X} \int_{t_i^X}^{t_{i+1}^X} f_{22}(t) dt, \\ &= \frac{\phi_{22}(t_{i+1}^X) - \phi_{22}(t_i^X)}{t_{i+1}^X - t_i^X}. \end{aligned} \quad (17)$$

The average frequency can then be defined as

$$\hat{f}_i(t) \equiv \hat{f}_{22,i}^p(t) + \hat{f}_{22,i}^a(t), \quad (18)$$

over the interval $t_i \leq t < t_{i+1}$. We refer the reader to [75, 98, 143, 144] for a detailed discussion on the orbit-averaging procedure. We interpolate $\hat{f}(t)$ with either a rational function or a linear fit. As also discussed in [75, 143], we observe that the average frequency \hat{f} and the mean frequency \bar{f} start to diverge on their approach to merger but agree in the early stages of the inspiral. This suggests that the impact of the explicit choice of the frequency parameter is subdominant in the determination of the eccentricity for simulations that have at least 3 – 4 complete orbits prior to the plunge.

The end-to-end procedure to calculate the eccentricity evolution e_{gw} is illustrated for our $q = 6$ simulation (ID:0028) in Fig. 4: In the upper panel, we show the highly oscillatory GW frequency (light blue), the periastron (orange dots) and apastron (blue dots), as well as the nonlinear rational fits, and the mean (pink) and average frequency (green). The bottom panel shows the resulting eccentricity measurement as a function of the mean frequency (pink) and the average frequency (green).

In the next section, we will discuss the robustness of this method to measure the eccentricity from NR simu-

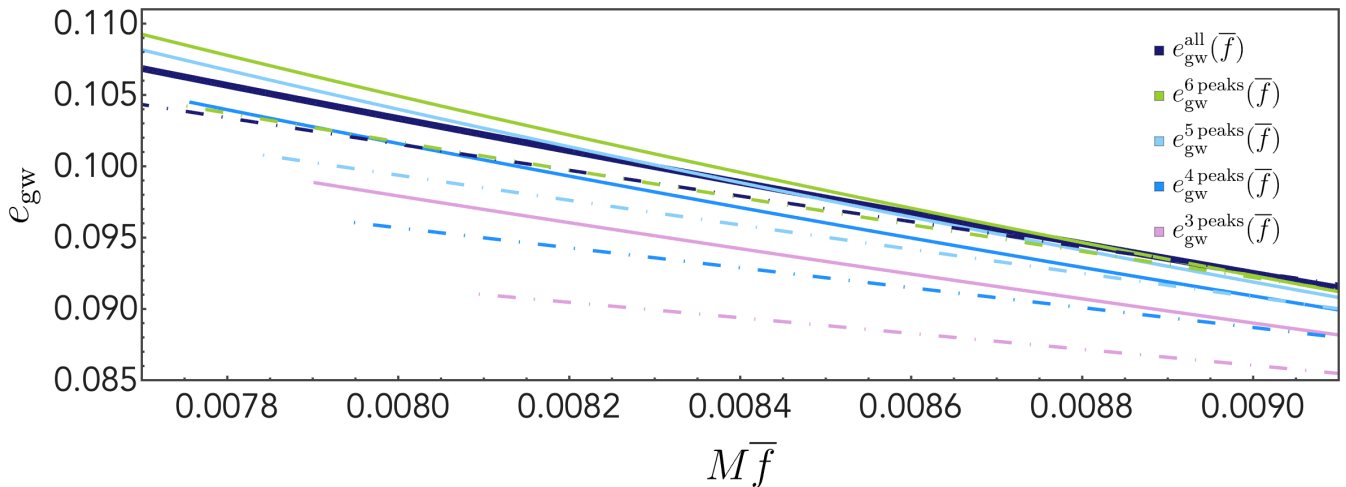


FIG. 5. Eccentricity evolution for ID:0028 as a function of mean frequency for different numbers of peaks. The dot-dashed lines show the evolution obtained retaining the last peak, the solid lines the evolution obtained when removing the last peak. The solid dark blue line is the reference baseline which includes all peaks except the last one. We observe that retaining the last peak (dot-dashed) usually leads to lower values of the inferred eccentricity reflecting the uncertainty in determining the eccentricity.

lations and possible sources of error.

C. Assessment of Robustness

1. Simulation Length

A crucial part of the eccentricity estimation are the fits to the apastra and periastra. However, the outcome depends on the choice of the domain that the fits are performed over. To obtain a robust measurement, and to safeguard against using the eccentricity estimator in a regime where it is no longer valid, we need to truncate the data before merger. We opt to remove the last ~ 4 GW cycles before merger from the data in agreement with [143], which allows us to remove all spurious peaks close to merger whilst retaining as much information as possible.

We assess the impact of the number of peaks included to infer the eccentricity evolution, which we find to be non-trivial. For the vast majority of our simulations, we found it beneficial to remove the last periastron and apastron. This is demonstrated in Fig. 5, where we show the eccentricity evolution, $e_{gw}(\bar{f})$, inferred with a varying number of peaks. Using our longest simulation with 28 GW cycles (ID:0028), we initially include all frequency peaks and sequentially omit peaks starting from the beginning. The solid (dot-dashed) lines represent the inferred eccentricity evolution when the last peak has been removed (retained). By comparing to the eccentricity curve that uses the most information (black line), we note that removing the last peak typically leads to a smaller spread in the estimated eccentricity relative to the evolution inferred when retaining the last peak. This is par-

ticularly prominent for short simulations that span fewer than ~ 15 GW cycles as the peaks closest to merger correspond to the regime where the GW frequency changes rapidly and can therefore shift the inferred eccentricity to higher or lower values, introducing inaccuracies in the inferred quantities. As we do not trust the estimator close to merger, and given the observed lack of robustness, we always remove the last peak when estimating the eccentricity.

2. Extrapolation vs. finite radius

Numerical relativity simulations often extract the GW signal at a series of finite radii, which are then extrapolated to future null infinity. This procedure can introduce errors, which can impact the eccentricity measurement.

In Fig. 6 we compare the eccentricity curves $e_{gw}(\bar{f})$ obtained from different extraction radii against those inferred using the extrapolated waveforms. We find very good agreement throughout the inspiral phase but see more differences during the later stages close to merger, as shown in the bottom panel. Our results suggest that one can use either finite radius waveforms or extrapolated waveforms to reliably compute the eccentricity evolution up to ~ 4 orbits before merger.

3. h vs. ψ_4

Until now, we have investigated the eccentricity estimated only from the (2,2)-mode of the gravitational-wave strain h . In this section, we use Ψ_4 to estimate the eccentricity, as this is often a directly measured quantity

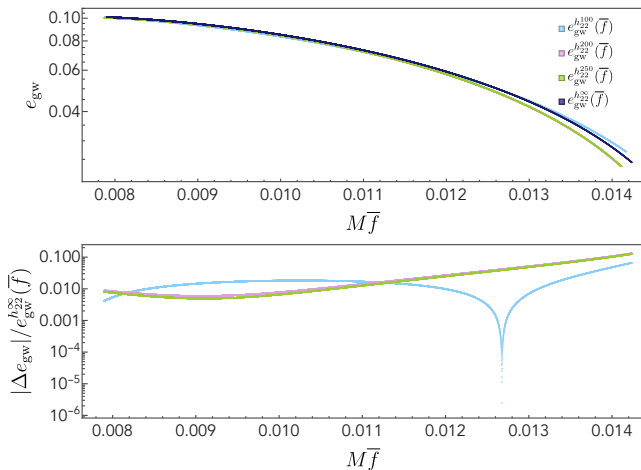


FIG. 6. Top panel: Eccentricity evolution computed for simulation ID:0002 for a series of finite extraction radii compared to the extrapolated waveform (dark blue). Bottom panel: The relative error, where $\Delta e_{\text{gw}} = e_{\text{gw}}^X - e_{\text{gw}}^{h^{\infty}}$, between the eccentricity inferred from the extrapolated waveform and the finite-radii waveforms. The curves agree for most of the inspiral phase up to around 4 orbits before merger, where we cut the data.

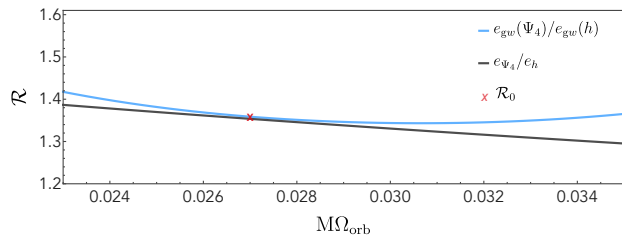


FIG. 7. Ratio \mathcal{R} between the eccentricity evolution computed employing Ψ_4 and eccentricity evolution computed employing h . The blue curve shows the ratio $e_{\text{gw}}(\Psi_4)/e_{\text{gw}}(h)$ as estimated from the numerical data. The black curve shows the ratio calculated from Eq. (19) and Eq. (20).

in NR data.

To estimate the eccentricity evolution from Ψ_4 , we use the same procedure as for h , described in Sec. III B. However, when using Ψ_4 , we apply a *trimmed mean* filter to the data to mitigate against numerical noise when calculating the derivative of the phase, which can induce errors in determining the positions of the apastra and periastra. Care needs to be taken when filtering the data to ensure that we do not introduce unphysical features, e.g. artificially shifting the time of the merger (see Appendix A).

An important subtlety is that the eccentricity measured from Ψ_4 differs from the eccentricity measured from h , e.g., see [148]. The eccentricity derived from the GW frequency of Ψ_4 and h can be analytically estimated to leading order in terms of an eccentric parameter e_t defined in the quasi-Keplerian parametrization [43]. At

1PN, we have

$$e_{\Psi_4} = \frac{7}{4}e_t - \epsilon x \left(\frac{125 + 52\nu}{168} \right) e_t, \quad (19)$$

$$e_h = e_t + \epsilon x \left(\frac{115 - 16\nu}{42} \right) e_t, \quad (20)$$

where e_{Ψ_4} is derived in the quasi-Keplerian parametrization in Appendix B and e_h is derived using Eq. (19) and (23) of [75], expanded for small eccentricities. In Eq. (19) and Eq. (20) $x = (M\Omega_{\text{orb}})^{2/3}$, and $\epsilon^2 = c^{-2}$ tracks the PN order. We can calculate the ratio between the two as a consistency check on the agreement between the eccentricity inferred from h and Ψ_4 ,

$$\mathcal{R} \equiv \frac{e_{\Psi_4}}{e_h} \quad (21)$$

and we see how this agrees at Newtonian order, with Eq. (C25) of [148]. In Fig. 7, we calculate the eccentricity evolution of ID:0016 using Ψ_4 and h and numerically calculate the ratio (blue curve). The black curve shows the analytical ratio in Eq. (21) derived from Eq. (19) and Eq. (20). The red cross indicates the value $\{M\Omega_{\text{orb}} = 0.027, \mathcal{R}_0 = 1.36\}$ calculated in [148], see Sec. II and Fig.(20) therein. We see how the value agrees with our computed ratios. The numerically and analytically estimated ratios agree reasonably well within a range of frequencies spanning $0.025 \lesssim M\Omega_{\text{orb}} \lesssim 0.029$. The disagreement at low- and high-frequencies is likely driven by a number of factors including numerical noise and the comparatively low PN order used for the estimators.

IV. COMPARISON TO ANALYTICAL MODELS

In this section, we compare our suite of NR simulations to an eccentric extension of the TEOBResumS model [154–157] known as TEOBResumS-DaLi [92–94, 103–105]. In this model, eccentricity is incorporated by dressing the circular azimuthal radiation reaction term with the Newtonian (leading-order) non-circular correction [92]. This modelling of eccentricity has been subsequently improved by incorporating higher order post-Newtonian information in a factorized and resummed form [94, 96, 97], building on the 2PN results presented in [58].

In the previous section we introduced a robust method for identifying pairs of mean frequency and eccentricity, $\{M\bar{f}, e_{\text{gw}}\}_{\text{NR}}$ at the first apastron from NR simulations. In this section we will now use the eccentricity evolution as a function of mean frequency to develop a robust procedure for directly comparing eccentric NR simulations with other waveform models that may use a different definition of eccentricity, which can obfuscate comparisons between different waveform models. The advantage of this is that we can perform these direct comparisons without the need for numerical optimisations over the eccentricity as was done in previous works, e.g [93, 94, 97, 98, 158]. We will demonstrate the efficacy

Numerical Relativity			TEOBResumS-DaLi		$\Delta\phi$ [rad]	Δt [M]
ID	$M\bar{f}_{\text{NR}}$	e_{NR}	$M\bar{f}_{\text{DALI}}$	e_{DALI}		
0001	0.0076203	0.0510486	0.00762334	0.0510313	0.439	1.64
0002	0.00853042	0.0980399	0.00852527	0.0980725	0.346	-1.78
0003	0.00853016	0.0993008	0.00853787	0.0992382	0.383	2.59
0004	0.00949267	0.116386	0.00937463	0.119877	0.319	-16.92
0005	0.00807595	0.0876158	0.00811259	0.0873528	-0.012	18.17
0006	0.0113294	0.186742	0.0111475	0.192453	0.053	-13.96
0007	0.0113196	0.1871	0.0111526	0.192687	0.098	-12.70
0008	-	-	-	-	-	-
0009	0.00987994	0.170253	0.00998654	0.16836	-0.426	24.35
0010	-	-	-	-	-	-
0011	0.00914328	0.0398909	0.00910584	0.0405297	0.195	-8.14
0012	0.00862177	0.0869213	0.00863143	0.0868591	0.490	3.17
0013	-	-	-	-	-	-
0014	0.00791276	0.053303	0.00793832	0.0531359	0.463	12.90
0015	0.00799565	0.0613589	0.00794926	0.0622875	0.211	-16.89
0016	0.00736959	0.0457956	0.0073548	0.0458236	-0.345	-16.40
0017	0.00845326	0.101092	0.00844698	0.101141	0.306	2.29
0018	0.00936701	0.11873	0.00925574	0.121864	0.018	-18.90
0019	0.00801989	0.0871244	0.00803822	0.087002	-0.40	11.03
0020	0.0074702	0.0533001	0.00747325	0.0532801	0.654	2.31
0021	0.00757658	0.0547304	0.00756598	0.0548007	0.725	-7.71
0022	0.00800259	0.0617299	0.00797527	0.0619813	0.452	-14.36
0023	0.00741632	0.0477771	0.00738662	0.0479505	-0.459	-30.35
0024	0.00834383	0.102726	0.00835499	0.102646	0.586	5.60
0025	0.00834383	0.102726	0.00835499	0.102646	0.586	5.60
0026	-	-	-	-	-	-
0027	0.00751769	0.0542868	0.00751769	0.0542868	0.499	-15.40
0028	0.00781405	0.105506	0.00777383	0.105979	1.326	-0.60
SXS:BBH:1358	0.00592098	0.152821	0.00595224	0.152033	0.509	52.10
SXS:BBH:1360	0.0065153	0.207213	0.00664508	0.202663	0.605	136.59

TABLE II. Summary of the eccentric initial conditions calculated for our set of NR simulations (were applicable) and for two SXS simulations. The first column indicates the simulation ID, the second and third columns give the eccentric initial conditions at first apastron in the NR data. The fourth and fifth columns give the values of the eccentric initial conditions calculated following our procedure. In last two columns we give the phase differences at merger as well as the time difference Δt . Simulations without values are too short to reliably determine the eccentricity evolution.

of our procedure for the new simulations listed in Tab. I as well as for a selected number of simulations from the SXS catalog [153] to compare against TEOBResumS-DaLi.

A. Determining Initial Conditions

We start by calculating the mean frequency and eccentricity evolution of the NR simulations that have at least two clear peaks in the waveform frequency using the method described in Sec. III B. We use the first apastron to set a reference time, t_{NR}^a , and denote the values of the

mean frequency and the eccentricity at the first apastron as $\{M\bar{f}, e\}_{\text{NR}}$. We then initialise TEOBResumS-DaLi with these values to generate the waveform to which we apply a time shift such that the merger occurs at the same time as in the corresponding NR waveform. Note that we choose $M\bar{f}$ for consistency with the definition of the monotonic frequency in TEOBResumS-DaLi, which is defined as $\bar{f}_{\text{TEOB}} = (f^a + f^p)/2$. However, the same procedure can be applied utilizing $M\hat{f}$.

After generating the TEOBResumS-DaLi waveform, we find that the time of its first apastron does not exactly correspond to t_{NR}^a . This offset is due to the following:

1) `TEOBResumS-Dalí` uses a different definition of the eccentricity, which is based on orbital quantities, while the gauge invariant estimator in Eq. (14) only depends on the waveform; 2) the eccentric initial conditions in `TEOBResumS-Dalí` are estimated using a post-adiabatic expansion [159] (see also Appendix A of [108]), which makes the model sensitive to changes in the frequency and eccentricities at the $\sim \mathcal{O}(10^{-6})$ level [93]. We determine the difference in the time of the apastron as

$$\Delta t = t_{\text{NR}}^a - t_{\text{TEOB}}^a, \quad (22)$$

and calculate a *new* pair of initial conditions defined at the time $t_{\text{NR}}^a + \Delta t$ such that $t_{\text{TEOB}}^a \simeq t_{\text{NR}}^a$. The procedure can be schematically written as:

1. Calculate $\{M\bar{f}, e_{\text{gw}}\}_{\text{NR}}$ at the time of the first apastron t_{NR}^a using the methodology described in Sec. III B.
2. Use $\{M\bar{f}, e_{\text{gw}}\}_{\text{NR}}$ to initialise `TEOBResumS-Dalí` and perform a time shift such that the `TEOBResumS-Dalí` merger time corresponds to the NR merger time.
3. Identify the time difference Δt between the first apastron in NR vs. `TEOBResumS-Dalí`.
4. Read off a new pair values at $t_{\text{NR}}^a + \Delta t$ and denote these $\{M\bar{f}, e_{\text{gw}}\}_{\text{DALI}}$.
5. Use $\{M\bar{f}, e_{\text{gw}}\}_{\text{DALI}}$ to initialise `TEOBResumS-Dalí`.
6. Perform an overall phase shift to align the phases at $t_{\text{TEOB}} = 0$.

We note that by specifying the initial conditions at the time of the first apastron for a given frequency, we are effectively fixing the mean anomaly. This provides a geometrically motivated picture for generating a set of self-consistent initial conditions. Other approaches, such as [93], numerically optimize over the eccentricity and frequency, making it difficult to meaningfully compare the dynamics in a transparent manner.

To validate our procedure for determining self-consistent initial conditions we apply it to a `TEOBResumS-Dalí` waveform with $\{q = 6, \chi_{1,z} = \chi_{2,z} = 0\}$ as shown in Fig. 8. In the upper panel, we see that the eccentricity evolution generated using the initial conditions calculated through our procedure (blue) closely matches the original evolution (purple) with phase differences smaller than 0.2 rad (bottom panel).

The result of applying this procedure to the suite of NR simulations is summarised in Tab. II. The initial conditions used to start the EOB dynamics closely resemble the initial conditions originally computed, with differences ranging from 10^{-6} to 10^{-4} for the frequency and 10^{-4} to 10^{-3} for the eccentricity. In Tab. II we also indicate the dephasing $\Delta\phi = \phi_{\text{NR}} - \phi_{\text{TEOB}}$ at the time

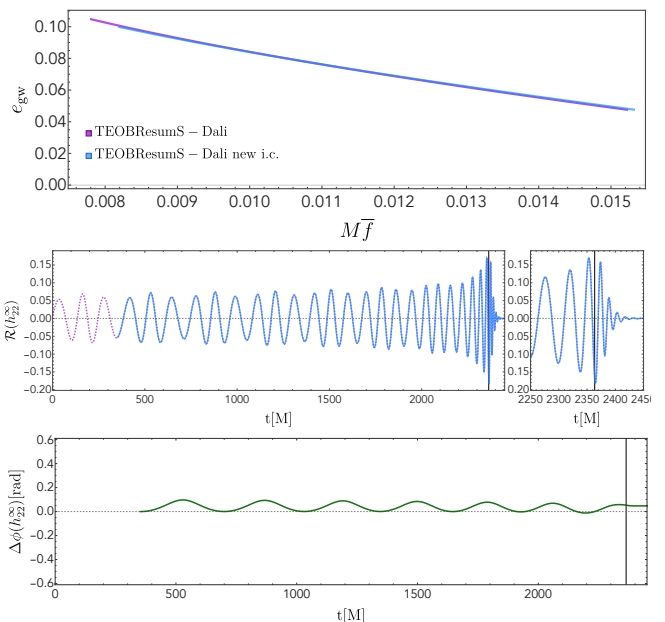


FIG. 8. Comparison between two `TEOBResumS-Dalí` waveforms to verify the proposed procedure to determine the initial conditions. The upper panel shows the eccentricity curves e_{gw} , the middle panel the waveforms and the bottom panel the phase differences. We find almost identical waveforms and oscillatory phase difference smaller than 0.2 rad.

of merger, which acts as a measure of the accumulated error.

A comparison between a subset of the NR simulations across the parameter space and `TEOBResumS-Dalí` waveforms is shown in Fig. 9. For each configuration the top panel shows the real part of h_{22}^{∞} of the NR waveform (purple, dashed) and the corresponding `TEOBResumS-Dalí` waveform (blue, solid); the bottom panel shows the dephasing $\Delta\phi$ with the maximum dephasing on the order of ~ 1.326 rad.

B. Robustness

We verify the reliability of the described procedure by testing a range of different assumptions, including: i) accounting for the last peak, ii) employing Ψ_4 instead of the strain h , iii) determining the initial conditions using the second apastron, and iv) considering finite extraction radii. The obtained initial conditions are summarised in Tab. III. Figure 10 illustrates the impact of the inclusion (exclusion) of the last peak, as well as the inclusion (exclusion) of the first peak for ID:0028. The two upper panels (10a and 10b) show the waveforms and phases obtained by retaining the first peak, the two bottom panels (10c and 10d) show the waveforms and phases obtained by removing the first peak. As expected from the study in Sec. III C 1, in both cases oscillatory phase differences are more pronounced and a larger phase shift is needed (see

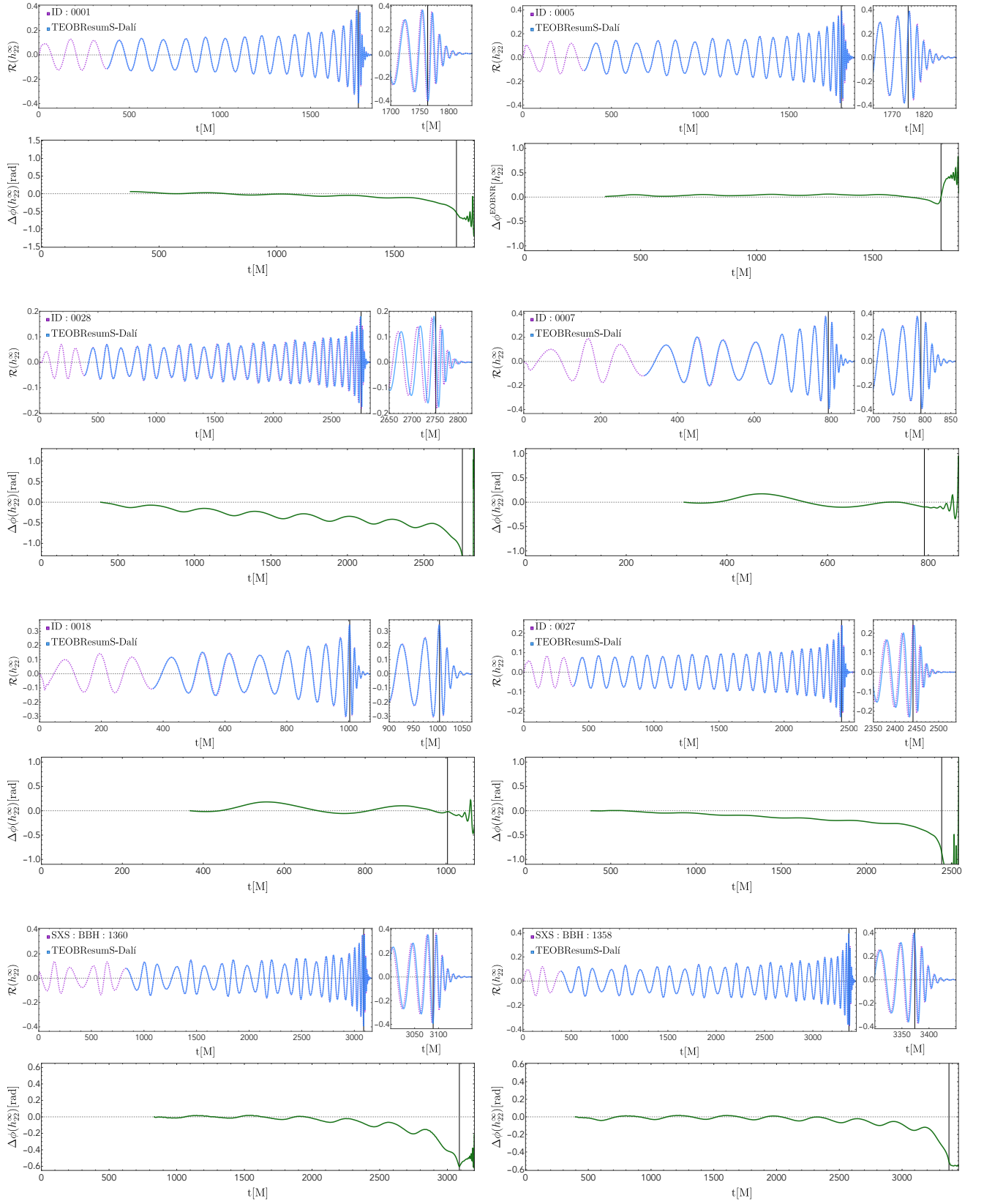


FIG. 9. Illustration of the ICs-finding procedure for a selection of NR simulations. For each simulation we show the NR (purple, dashed) and `TEOBResumS-Dalí` (blue, solid) waveforms in the top panel with a zoom-in of the merger part on the right. The bottom panel shows the phase difference. We see that the EOB waveforms generated with the initial conditions as determined by the procedure described in Sec. IV A closely match the NR waveforms; the phase differences are less than ~ 1 rad at merger.

Tab. III) when including the last peak (right panels) than when removing it (left panels). On the other hand, it can sometimes be advantageous to start the EOB dynamics at the second peak as the first peak can be affected by numerical noise, making the eccentricity estimation more prone to errors. We demonstrate that our procedure is capable of handling such noise artifacts by applying it starting from the second apastron instead. As expected, we obtain slightly different initial conditions but find a very similar maximal dephasing at merger. As before, the largest phase error is seen when also including the last peak.

As shown previously in Fig. 6 for ID:0002, waveforms extracted at a finite radius rather than extrapolated to infinity yield a slightly different eccentricity evolution, resulting in a small change in initial conditions. We find that the smallest extraction radii lead to the largest dephasing at merger, while the extrapolated waveforms give the best agreement with `TEOBResumS-Da11`.

Finally, we also test the procedure using Ψ_4 instead of the strain. This can be useful when the waveform extraction procedure is particularly challenging or affected by numerical noise. This approach allows indeed to compute the eccentricity evolution directly from Ψ_4 by simply using the ratio Eq. (21). Employing the latter we calculate the ratio $\mathcal{R}(\bar{\omega}_{\text{NR}}/2)$ where $\bar{\omega}_{\text{NR}} = 2\pi f_{\text{NR}}$ for ID:0016 at the frequency of first apastron to be 1.385. The initial eccentricity is then calculated as

$$e_{\text{NR}} = \frac{e_{\text{gw}}(\Psi_4)}{\mathcal{R}}. \quad (23)$$

The phase differences obtained using Ψ_4 are very similar to the ones obtained from h , see Tab. III. This suggests that the procedure is equally applicable to Ψ_4 and h .

Overall, we find that our procedure is robust and gives self-consistent results for the various assumptions made.

C. Extrapolation to Earlier Times

A limitation of this procedure is that we define a reference time based on the first apastron in the data. When using NR simulations, for example, this results in a loss of $\sim 300 - 400M$ at the start of the simulation. We could start the evolution from an earlier time using, e.g., a backwards PN evolution or, alternatively, we could try to extrapolate the initial conditions. In this section we test the extrapolation of the initial conditions, demonstrating that we can robustly generate a waveform from earlier times.

Using `SXS:BBH:1360`, we want our waveform to start at $t_{\text{NR}} = 0$. However, this requires determining initial conditions for an apastron that occurs before $t_{\text{NR}} = 0$. As we do not know the exact location of the apastron at earlier times, we empirically estimate it using the periastron advance as a guide, e.g., we find $t_{\text{NR}}^a \sim -63M$ for `SXS:BBH:1360`. The procedure laid out in Sec. IV A is then slightly modified:

1. Read off the NR initial conditions at $t_{\text{NR}}^a + \Delta t$, taking Δt to be the time difference already found and listed in Tab. II. This constitutes our original initial conditions, as listed in columns two and three of Tab. III.
2. We then iterate the procedure to find new initial conditions based on the original values identified in 1) to help mitigate against the fact that the apastron was only estimated empirically, therefore allowing for a more precise measurement of the initial conditions.

The initial conditions, phase difference and the final Δt are listed in the last row of Tab. III. The total time difference between the NR and the EOB evolution is given by the sum of the time differences listed in Tab. II and Tab. III. The resulting waveforms and dephasing are shown in Fig. 11. We see that the phases differences are larger compared to Fig. 9 but the dephasing is still quite small, with a maximum of 0.645 rad at merger. Whilst this procedure is promising, the robustness of extrapolating to earlier times needs to be carefully checked across the parameter space.

D. Mismatches

In order to quantify the (dis)agreement between the NR simulations and the `TEOBResumS-Da11` waveforms, we use the match \mathcal{M} , defined in the usual way as

$$\mathcal{M}(h_{\text{NR}}, h_{\text{TEOB}}) = \max_{t_c, \phi_c} \frac{\langle h_{\text{NR}} | h_{\text{TEOB}} \rangle}{\sqrt{\langle h_{\text{NR}} | h_{\text{NR}} \rangle \langle h_{\text{TEOB}} | h_{\text{TEOB}} \rangle}}, \quad (24)$$

where t_c and ϕ_c denote the time and phase of coalescence respectively, and $\langle h_{\text{NR}} | h_{\text{TEOB}} \rangle$ denotes a noise-weighted inner product

$$\langle h_{\text{NR}} | h_{\text{TEOB}} \rangle = 4\Re \int_{f_{\text{min}}}^{f_{\text{max}}} \frac{\tilde{h}_{\text{NR}}(f) \tilde{h}_{\text{TEOB}}^*(f)}{S_n(|f|)} df, \quad (25)$$

where $S_n(|f|)$ is the one-sided power spectral density (PSD) of the strain noise, \tilde{h} the Fourier transform of h and $*$ denotes the complex conjugate. In practice, we will use the mismatch, which is defined as

$$\overline{\mathcal{M}}(h_{\text{NR}}, h_{\text{TEOB}}) = 1 - \mathcal{M}(h_{\text{NR}}, h_{\text{TEOB}}) \quad (26)$$

where $h_{\text{NR}} \equiv h_{22}^{\infty}$ from the numerical data.

The mismatches are computed assuming $f_{\text{min}} = 20$ Hz and a total mass M in the range $[50, 200]M_{\odot}$. We use a PSD that corresponds to the approximate sensitivity of the Advanced LIGO detector in the fourth observing run (O4) [160, 161]. The resulting mismatches are shown in Fig. 12. We find good agreement between the NR and EOB waveforms across the parameter space spanned by our simulations, with a typical mismatch on the order of $\sim \mathcal{O}(10^{-3})$. We do not find any strong correlations with

Numerical Relativity			TEOBResumS-Dali		$\Delta\phi$ [rad]	Δt [M]
ID	$M\bar{f}_{\text{NR}}$	e_{NR}	$M\bar{f}_{\text{DALI}}$	e_{DALI}		
0001	0.0076203	0.0510486	0.00762334	0.0510313	0.439	1.64
0001 (incl. last peak)	0.00765019	0.048717	0.00762572	0.0487785	0.461	-14.86
0002	0.00853042	0.0980399	0.00852527	0.0980725	0.346	-1.78
0002 ($r_0 = 100$ M)	0.00851419	0.0970785	0.0085116	0.0970969	0.636	-0.87
0002 ($r_0 = 200$ M)	0.00851574	0.0974921	0.00851574	0.0974921	0.511	1.56
0002 ($r_0 = 250$ M)	0.00851735	0.0975702	0.00852125	0.0975467	0.403	1.31
0016	0.00736959	0.0457956	0.0073548	0.0458236	-0.345	-16.40
0016 (Ψ_4)	0.00738382	0.046704	0.00734072	0.0468821	-0.483	-38.83
0028	0.00781405	0.105506	0.00777383	0.105979	1.326	-44.02
0028 (incl. last peak)	0.00827036	0.0990475	0.00820059	0.0997272	1.285	-70.19
0028 (2 nd apastron)	0.00822478	0.101856	0.00818341	0.102409	1.285	-36.69
0028 (2 nd apastron, incl. last peak)	0.0078723	0.102723	0.00779677	0.103425	1.504	-96.02
SXS:BBH:1360 (earlier time)	0.00598258	0.228105	0.00597789	0.228307	0.645	-8.28

TABLE III. Summary of initial conditions calculated under different assumptions: Varying number of peaks, using Ψ_4 instead of h and different finite extraction radii. The last row gives the initial conditions inferred when extrapolating to earlier times.

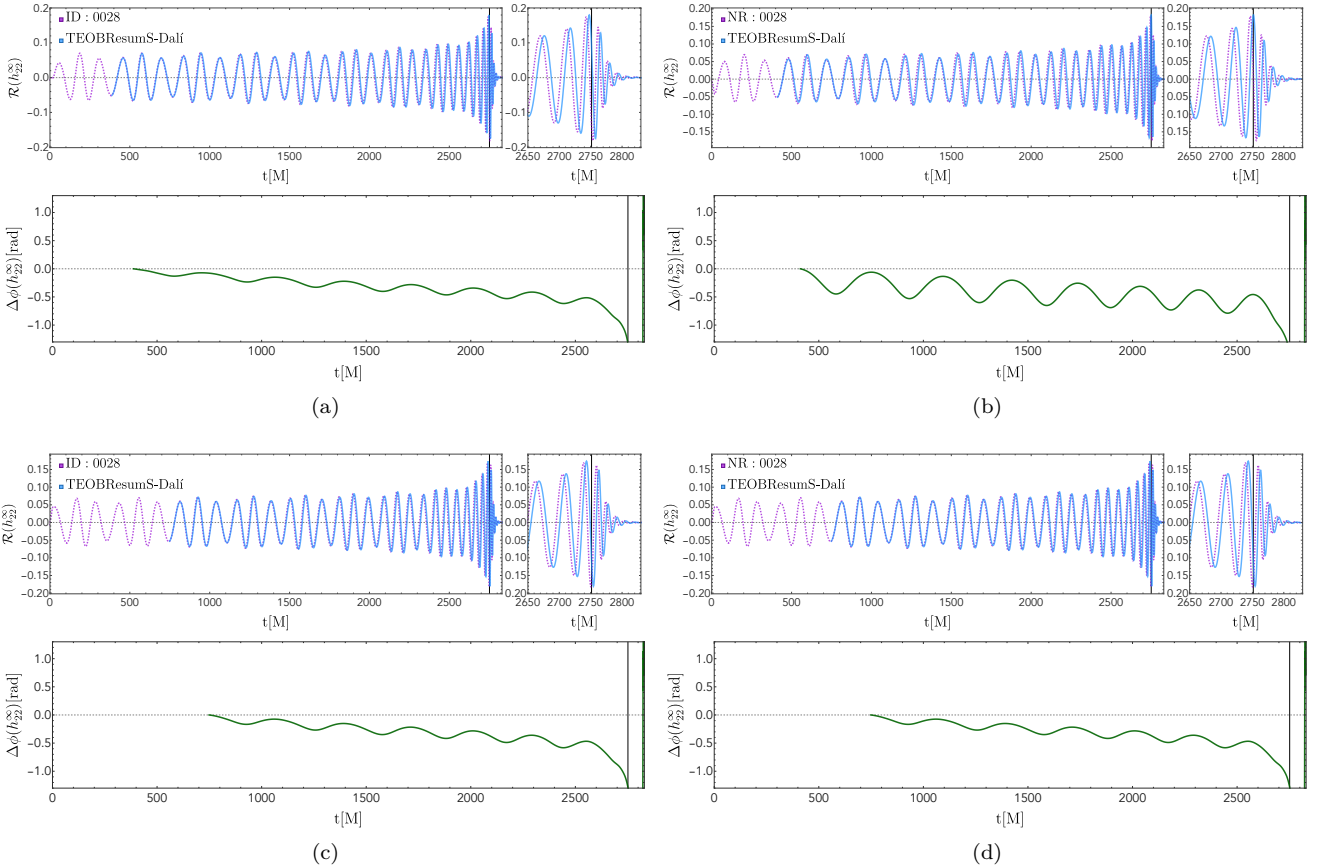


FIG. 10. Here we explore the impact of including the last peak using simulation ID:0028. The two upper panels (a and b) show the waveforms and phases differences obtained when retaining the *first* peak. The bottom two panels (c and d) are when we exclude the *first* peak from the estimation. The left panels (a and c) are obtained by *removing* the last peak, whereas the right panels (b and d) are obtained by *including* the last peak. We generally observe larger oscillatory phase differences when we include the last peak, i.e., the right panels.

q , e_0 and χ_{eff} but note that the worst mismatches between our NR data and TEOBResumS-Dali waveforms are

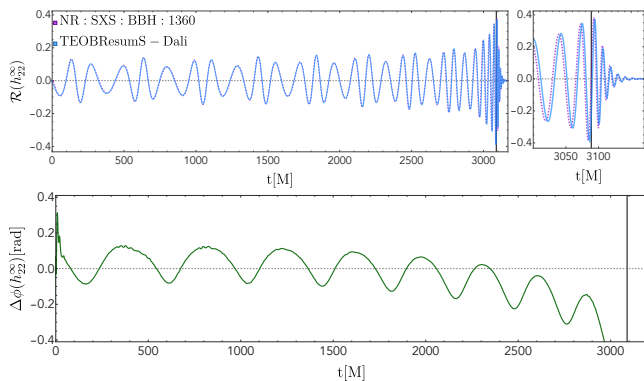


FIG. 11. Comparison of **SXS:BBH:1360** (purple) and **TEOBResumS-Dali** (blue) using the end-to-end pipeline to calculate the initial conditions at earlier times, as described in Sec. IV C, together with the phase difference (lower panel).

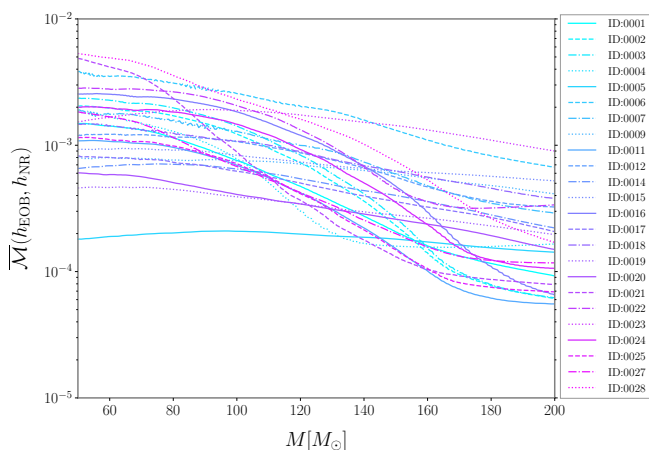


FIG. 12. Mismatches between our suite of numerical simulations and **TEOBResumS-Dali** across a range of total masses. The mismatches vary between a few times 10^{-3} to just below 10^{-4} . For binaries with a total mass of $65M_{\odot}$ the mean mismatch across our simulations is 0.0015.

found for unequal masses and large eccentricities. Our result is in broad agreement with [93] but it is crucial to note that, as opposed to other works, we have not performed any optimisations over eccentricity parameters as this is not necessary due to the identified mapping between initial conditions. This allows us to treat the orbital eccentricity as a meaningful physical parameter that characterises the binary rather than as a nuisance parameter that is numerically optimised over.

V. CONCLUSIONS

The primary goal of this work was to establish and validate a robust framework for defining a map between the eccentricity evolution as measured directly from a GW signal and eccentric initial conditions to allow for a direct comparison between different eccentric waveform models.

Our framework builds on [108] in terms of the eccentricity estimator e_{gw} recently introduced in [75], which has the correct Newtonian limit and is defined purely in terms of observables from the GW signal. The pipeline can be applied to any generic waveform data, including NR simulations and semi-analytic waveform models. In support of the analysis, we introduced a suite of 28 aligned-spin, eccentric NR simulations for binary black hole mergers, designed to help us understand the dynamics of eccentric binaries. We validated our pipeline against this catalog of NR simulations, as well as publicly available SXS simulations.

A crucial ingredient is the measurement of the eccentricity evolution. To assess its robustness, we systematically tested a number of possible limitations. In particular, we investigated how the number of peaks in the GW signal, the data quality, extrapolation to future null infinity, and the use of Ψ_4 versus the strain h impacted our ability to infer the eccentricity evolution from the NR simulations. As a result, we found that the minimum length of an NR simulation required to accurately measure the eccentricity evolution is ~ 15 GW cycles (~ 7 orbits). Similarly, we found that the procedure breaks down as the binary approaches merger and is unreliable ~ 4 GW cycles (~ 2 orbits) before merger, see also the discussion in [143]. In testing the pipeline, we also found that dropping the last peak from the fitting procedure results in a more reliable determination of the eccentricity, as discussed in Sec. III B, see also Fig. 10. Furthermore, our procedure can be defined using various definitions of (monotonic) frequency, including the mean frequency and the average frequency, also in agreement with [143].

With a reliable procedure for determining e_{gw} in place, we presented a simple framework for mapping eccentric initial conditions between NR simulations and EOB models in Sec. IV A. When performing comparisons between NR simulations against **TEOBResumS-Dali**, we found that we needed to account for a time shift between the NR and EOB waveforms before we could construct a map between the initial conditions. Nevertheless, after accounting for this time shift, we found excellent agreement between the NR and EOB initial conditions, resulting in waveforms with typical mismatches on the order of $\sim 10^{-3}$, as shown in Fig. 12. We also verified that the determination of the initial conditions is robust under different options for the input data such as waveform extrapolation, finite extraction radii or the use of Ψ_4 , finding that the least dephasing is achieved when determining the eccentricity evolution from the extrapolated strain and excluding the last apastron peak in the fitting procedure. Utilising the periastron advance as an empirical estimator, we were also able to extrapolate our procedure to earlier times, allowing us to retain more of the NR data.

A key advantage of our framework is that we no longer need to perform any numerical optimisation over eccentric parameters but it instead appeals to geometrically meaningful initial conditions. A key practical application

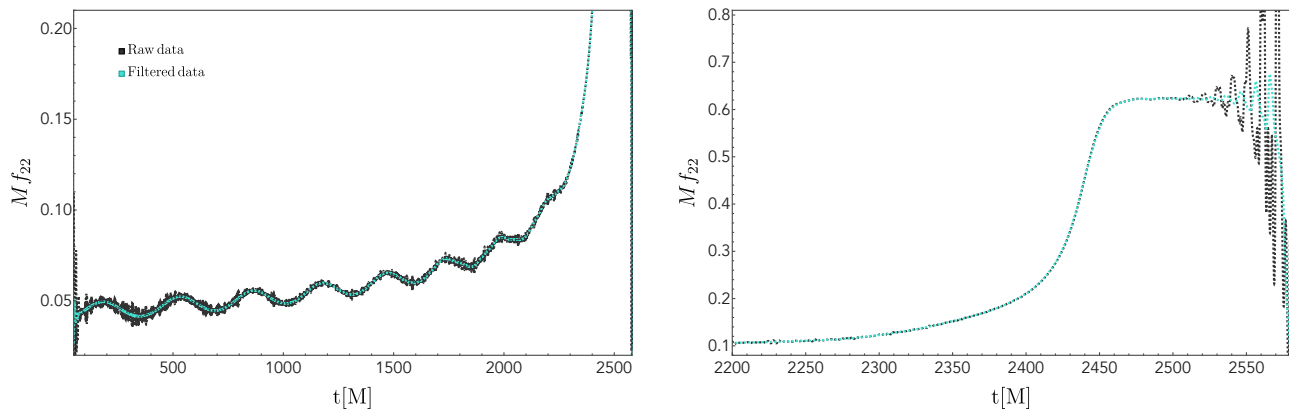


FIG. 13. Noise filtering of Ψ_4 . When filtering the data, we need to be careful to not introduce unphysical features or behaviour.

of this approach is towards calibrating an EOB model, in which the eccentricity evolution is matched to that of a corresponding NR simulation in terms of the same $\{M\bar{f}, e_{\text{gw}}\}$ pair. We will leave this for future work.

ACKNOWLEDGEMENTS

The authors thank Antoni Ramos-Buades, Md Arif Shaikh, Vijay Varma, Alessandro Nagar and Rossella Gamba for useful discussions. We also thank Gregorio Carullo for useful comments. A.B. is supported by STFC, the School of Physics and Astronomy at the University of Birmingham and the Birmingham Institute for Gravitational Wave Astronomy. G.P. is very grateful for support from a Royal Society University Research Fellowship URF\R1\221500 and RF\ERE\221015. GP gratefully acknowledges support from an NVIDIA Academic Hardware Grant. G.P. and P.S. acknowledge support from STFC grant ST/V005677/1. P.S. also acknowledges support from a Royal Society Research Grant RG\R1\241327. Numerical simulations and computations were performed using the University of Birmingham’s BlueBEAR HPC service, which provides a High Performance Computing service to the University’s research community, the Sulis Tier 2 HPC platform hosted by the Scientific Computing Research Technology Platform at the University of Warwick funded by EPSRC Grant EP/T022108/1 and the HPC Midlands+ consortium, and on the Bondi HPC cluster at the Birmingham Institute for Gravitational Wave Astronomy. This work also used the DiRAC@Durham facility managed by the Institute for Computational Cosmology on behalf of the STFC DiRAC HPC Facility (www.dirac.ac.uk).

The equipment was funded by BEIS capital funding via STFC capital grants ST/P002293/1, ST/R002371/1 and ST/S002502/1, Durham University and STFC operations grant ST/R000832/1. DiRAC is part of the National e-Infrastructure. Processing of the NR data was performed with Wolfram’s *Mathematica* [162] and *SimulationTools*, a package written by Ian Hinder and Barry Wardell, with contributions from Kyriaki Dionysopoulou and Aaryn Tonita. *Matplotlib* [163] was used for some of the visualisations. The version of *TEOBResumS-Da11* used in the comparisons corresponds to git commit bac2c08 [164]. This manuscript has the the LIGO document number P2400141.

Appendix A: Filtering of Ψ_4 and choice of ω_0

In this section we illustrate other possible errors that may occur when we apply the procedure described in Sec. III. In Fig. 13, we illustrate our filtering of Ψ_4 , noting that due care needs to be taken not to introduce unphysical features into the data. Figure 14 shows how the eccentricity evolution depends on the choice of cut-off frequency ω_0 for ID:0001. The evolution is strongly dependent on the choice of ω_0 and this can introduce large numerical errors. As discussed in Sec. III B, taking $\omega_0 = \omega_{22}^p/2$ was found to be a robust choice for the cutoff frequency entering the FFI.

We also checked the agreement between the strain extracted from the multipole moments $\Psi_{4,\ell m}$ and the one directly calculated from the metric perturbations via the Regge-Wheeler-Zerilli equations (as discussed in Sec. III B) finding that small variations in ω_0 only have a small impact on h constructed using FFI as shown in Fig. 15.

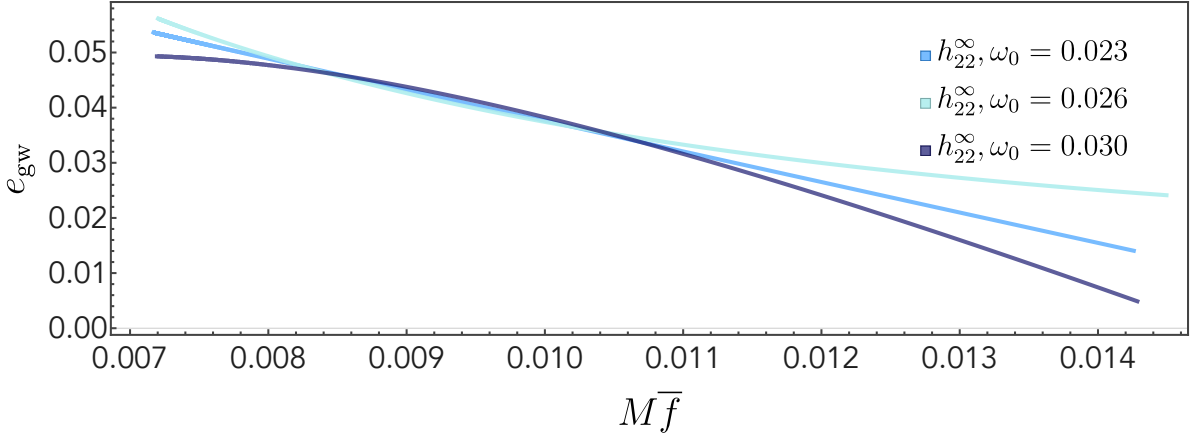


FIG. 14. Eccentricity curves for ID:0001 obtained by varying the FFI cutoff ω_0 . We note how the eccentricity evolution is dependent on the choice of the parameter.

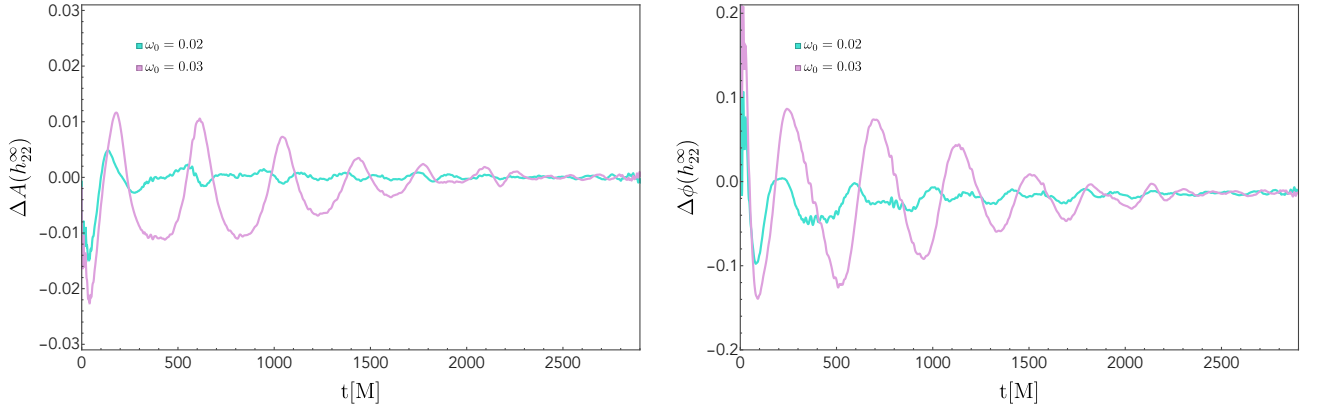


FIG. 15. Test of consistency between the strain extracted from the multipoles of the Newman-Penrose scalar, $\Psi_{4,\ell m}$, and the one calculated from the metric perturbations via the Regge-Wheeler-Zerilli equations (as discussed in Sec. III B), using SXS:BBH:1360. The left (right) panel shows the differences $\Delta A(h_{22}^\infty) = A_{22}^{\text{RWZ}} - A_{22}^{\text{FFI}}$ ($\Delta\phi(h_{22}^\infty) = \phi_{22}^{\text{RWZ}} - \phi_{22}^{\text{FFI}}$) between the amplitudes (phases) calculated using the RWZ formalism and the ones extracted from $\Psi_{4,\ell m}$ for different values of ω_0 . Different values of ω_0 have a small impact on the h_{22}^∞ inferred using the FFI, leading to a maximum difference after junk radiation of ~ -0.02 for the amplitudes and ~ -0.15 rad for the phases. We note that the waveform data were also extrapolated.

Appendix B: Derivation of e_{Ψ_4} in the quasi-Keplerian parametrization

In this appendix we derive the eccentricity estimator from the Newman-Penrose Weyl scalar Ψ_4 in Eq. (19) following the procedure to derive the eccentricity estimator from the waveform in the quasi-Keplerian parametrization described in Appendix C of [75]. We start from the expression for the (2, 2)-mode of the waveform h_{22}^{QK} given by Eq.(C26-C28) of [75] and compute $\Psi_4 \equiv -\ddot{h}$. The time derivatives of x , e_t , the mean anomaly l and the phase of the (2, 2)-mode of the waveform $\phi \equiv \phi_{22}$ at 1PN are found in [44, 165] and the Kepler equation for the eccentric anomaly u at Newtonian order is given by [75]

$$\dot{u} = \frac{\dot{l} + \dot{e}_t \sin u}{1 - e_t \cos u}, \quad (\text{B1})$$

with higher-order corrections entering at 2PN.

The time derivatives of $h_{22}^{\text{QK}}(x, e_t, u, l, \phi)$ are expressed as

$$\dot{h}_{22}^{\text{1PN}} \equiv \frac{dh_{22}^{\text{QK}}}{dt} = \frac{\partial h_{22}^{\text{QK}}}{\partial x} \dot{x} + \frac{\partial h_{22}^{\text{QK}}}{\partial e_t} \dot{e}_t + \frac{\partial h_{22}^{\text{QK}}}{\partial u} \dot{u} + \frac{\partial h_{22}^{\text{QK}}}{\partial l} \dot{l} + \frac{\partial h_{22}^{\text{QK}}}{\partial \phi} \dot{\phi}, \quad (\text{B2})$$

$$\ddot{h}_{22}^{1\text{PN}} \equiv \frac{dh_{22}^{1\text{PN}}}{dt} = \frac{\partial h_{22}^{1\text{PN}}}{\partial x} \dot{x} + \frac{\partial h_{22}^{1\text{PN}}}{\partial e_t} \dot{e}_t + \frac{\partial h_{22}^{1\text{PN}}}{\partial u} \dot{u} + \frac{\partial h_{22}^{1\text{PN}}}{\partial l} \dot{l} + \frac{\partial h_{22}^{1\text{PN}}}{\partial \phi} \dot{\phi}. \quad (\text{B3})$$

The 1PN expressions for $\Psi_{4,22}^{\text{QK}}$ can be written as

$$\Psi_{4,22}^{\text{QK}} = 4\nu x^4 \sqrt{\frac{\pi}{5}} \left[\hat{\Psi}_{4,22}^{0\text{PN}} + \epsilon \hat{\Psi}_{4,22}^{1\text{PN}} \right] e^{-2i\phi}, \quad (\text{B4})$$

$$\hat{\Psi}_{4,22}^{0\text{PN}} = \frac{-8 + e_t \cos(u) + e_t^2 (6 + \cos(2u)) + i10e_t \sqrt{1 - e_t^2} \sin(u)}{(e_t \cos(u) - 1)^5}, \quad (\text{B5})$$

$$\begin{aligned} \hat{\Psi}_{4,22}^{1\text{PN}} = & \frac{x}{168 (1 - e_t^2)^{3/2} (e_t \cos(u) - 1)^7} \left\{ \nu (e_t^2 - 1) \left[\sqrt{1 - e_t^2} (e_t^4 (-338 \cos(2u) + 17 \cos(4u) + 149) - e_t^3 (485 \cos(u) \right. \right. \\ & + 87 \cos(3u)) + 4e_t^2 (424 \cos(2u) + 431) - 4436e_t \cos(u) + 1760) \\ & \left. \left. - 14ie_t \left(e_t \left[e_t (81 - 191e_t^2) \sin(u) + 5e_t (5e_t^2 + 1) \sin(3u) + 8 (16e_t^2 - 31) \sin(2u) \right] + 260 \sin(u) \right) \right] \right. \\ & + 14ie_t (e_t^2 - 1) \left[e_t \left(e_t (845 - 423e_t^2) \sin(u) + 45e_t (e_t^2 + 5) \sin(3u) + 4 (17e_t^2 - 287) \sin(2u) \right) + 928 \sin(u) \right] \\ & + e_t \sqrt{1 - e_t^2} \left[e_t^3 \left(-57e_t^2 (\cos(4u) + 45) + 1107e_t \cos(3u) + 6 (515e_t^2 - 2227) \cos(2u) - 279 \cos(4u) - 5999 \right) \right. \\ & \left. \left. + e_t (-99e_t \cos(3u) + 10944 \cos(2u) + 10180) + (6737e_t^4 + 3851e_t^2 - 16972) \cos(u) \right] + 3424 \sqrt{1 - e_t^2} \right\}. \quad (\text{B6}) \end{aligned}$$

The phase of Eq. (B4) can be written as

$$\phi_{22}^{1\text{PN}} = \hat{\phi}^{0\text{PN}}(\Psi_{4,22}^{\text{QK}}) + \epsilon \hat{\phi}^{1\text{PN}}(\Psi_{4,22}^{\text{QK}}), \quad (\text{B7})$$

$$\hat{\phi}^{0\text{PN}}(\Psi_{4,22}^{\text{QK}}) = \text{Arctan} \left[\frac{20e_t (e_t^2 - 1) \sin(u) \cos(2\phi) + 2\sqrt{1 - e_t^2} \sin(2\phi) (6e_t^2 + e_t (e_t \cos(2u) + \cos(u)) - 8)}{20e_t (e_t^2 - 1) \sin(u) \sin(2\phi) - 2\sqrt{1 - e_t^2} \cos(2\phi) (6e_t^2 + e_t (e_t \cos(2u) + \cos(u)) - 8)} \right], \quad (\text{B8})$$

$$\hat{\phi}^{1\text{PN}}(\Psi_{4,22}^{\text{QK}}) = \frac{A}{B}, \quad (\text{B9})$$

where

$$\begin{aligned} A = & xe_t \left[2 \sin(u) \left((18339 - 4428\nu)e_t^6 + (5745\nu - 30328)e_t^4 + (93\nu - 3965)e_t^2 - 2880\nu + 17424 \right) \right. \\ & + e_t \left[2 \sin(2u) \left(e_t^2 \left((2895\nu - 7804)e_t^2 - 3594\nu + 19202 \right) + 1854\nu - 12553 \right) \right. \\ & + e_t \left(15e_t^2 \sin(5u) \left((3\nu - 1)e_t^2 + 4\nu - 6 \right) + e_t \sin(4u) \left((753\nu - 3163)e_t^2 - 1068\nu + 3478 \right) \right. \\ & \left. \left. \left. + \sin(3u) \left(e_t^2 \left(3(423\nu - 2759)e_t^2 - 5586\nu + 22582 \right) + 4002\nu - 13990 \right) \right) \right] \right], \quad (\text{B10}) \end{aligned}$$

$$B = 42 \sqrt{1 - e_t^2} (e_t \cos(u) - 1)^2 \left[e_t \left[(26e_t^2 - 32) \cos(u) + e_t (e_t (e_t \cos(4u) + 2 \cos(3u)) \right. \right. \right.$$

$$+ \left(124e_t^2 - 131 \right) \cos(2u) \Big] - 27e_t^4 - 91e_t^2 + 128 \Big]. \quad (\text{B11})$$

The frequency of $\Psi_{4,22}^{\text{QK}}$ can be expressed as the derivative of the Eq. (B7) as

$$\omega_{22}^{1\text{PN}} \equiv \frac{d\phi_{22}^{1\text{PN}}}{dt} = \frac{\partial\phi_{22}^{1\text{PN}}}{\partial x} \dot{x} + \frac{\partial\phi_{22}^{1\text{PN}}}{\partial e_t} \dot{e}_t + \frac{\partial\phi_{22}^{1\text{PN}}}{\partial u} \dot{u} + \frac{\partial\phi_{22}^{1\text{PN}}}{\partial l} \dot{l} + \frac{\partial\phi_{22}^{1\text{PN}}}{\partial \phi} \dot{\phi}. \quad (\text{B12})$$

At the turning points, periastron ($u = 0$) and apastron ($u = \pi$), the (2, 2)-waveform frequency at 1PN can be written as

$$\begin{aligned} \omega_{22,p}^{1\text{PN}} &= \frac{8(e_t + 1)(2 + 3e_t)}{\sqrt{1 - e_t^2} (7e_t^2 + e_t - 8)} x^{3/2} \\ &+ \epsilon e_t x^{5/2} \frac{(9(134\nu - 327)e_t^3 + (2028\nu - 6094)e_t^2 + (2238\nu - 823)e_t + 24(52\nu + 125))}{21\sqrt{1 - e_t^2} (7e_t^2 + e_t - 8)^2}, \end{aligned} \quad (\text{B13})$$

and

$$\begin{aligned} \omega_{22,a}^{1\text{PN}} &= \frac{8(2 - 3e_t)\sqrt{1 - e_t}}{(1 + e_t)^{3/2}(7e_t - 8)} x^{3/2} \\ &+ \epsilon e_t x^{5/2} \frac{\sqrt{1 - e_t^2} (-9(134\nu - 327)e_t^3 + (2028\nu - 6094)e_t^2 + (823 - 2238\nu)e_t + 24(52\nu + 125))}{21(8 - 7e_t)^2 (e_t - 1) (e_t + 1)^3}. \end{aligned} \quad (\text{B14})$$

Substituting Eq. (B14) and Eq. (B15) into Eq. (13), and expanding up to 1PN, we find

$$\begin{aligned} e_{\omega_{22}}(\Psi_4) &= \frac{21e_t^4 - \left(\sqrt{441e_t^4 - 772e_t^2 + 256} + 15 \right) e_t^2 + \sqrt{441e_t^4 - 772e_t^2 + 256} - 16}{32e_t^3 - 42e_t} \\ &- \frac{x \left(e_t (30(54\nu + 269)e_t^4 + (13194\nu + 1615)e_t^2 - 192(52\nu + 125)) \right)}{84 \left(\sqrt{441e_t^4 - 772e_t^2 + 256} \left(21e_t^4 + \left(\sqrt{441e_t^4 - 772e_t^2 + 256} - 15 \right) e_t^2 - \sqrt{441e_t^4 - 772e_t^2 + 256} - 16 \right) \right)}. \end{aligned} \quad (\text{B15})$$

Substituting in Eq. (14) and Eq. (15) and expanding for small eccentricities we obtain Eq. (19)

$$e_{\Psi_4} = \frac{7}{4} e_t - \epsilon x e_t \left(\frac{52\nu + 125}{168} \right). \quad (\text{B16})$$

-
- [1] I. Mandel and A. Farmer, Merging stellar-mass binary black holes, *Phys. Rept.* **955**, 1 (2022), [arXiv:1806.05820 \[astro-ph.HE\]](#).
- [2] M. Mapelli, Binary Black Hole Mergers: Formation and Populations, *Front. Astron. Space Sci.* **7**, 38 (2020), [arXiv:2105.12455 \[astro-ph.HE\]](#).
- [3] I. Mandel and F. S. Broekgaarden, Rates of compact object coalescences, *Living Rev. Rel.* **25**, 1 (2022), [arXiv:2107.14239 \[astro-ph.HE\]](#).
- [4] M. Mapelli, Formation Channels of Single and Binary Stellar-Mass Black Holes (2021) [arXiv:2106.00699 \[astro-ph.HE\]](#).
- [5] C. L. Rodriguez, M. Zevin, C. Pankow, V. Kalogera, and F. A. Rasio, Illuminating Black Hole Binary Formation Channels with Spins in Advanced LIGO, *Astrophys. J. Lett.* **832**, L2 (2016), [arXiv:1609.05916 \[astro-ph.HE\]](#).
- [6] W. M. Farr, S. Stevenson, M. Coleman Miller, I. Mandel, B. Farr, and A. Vecchio, Distinguishing Spin-Aligned and Isotropic Black Hole Populations With Gravitational Waves, *Nature* **548**, 426 (2017), [arXiv:1706.01385 \[astro-ph.HE\]](#).
- [7] M. Zevin, C. Pankow, C. L. Rodriguez, L. Sampson, E. Chase, V. Kalogera, and F. A. Rasio, Constraining Formation Models of Binary Black Holes with Gravitational-Wave Observations, *Astrophys. J.* **846**, 82 (2017), [arXiv:1704.07379 \[astro-ph.HE\]](#).
- [8] M. Zevin, S. S. Bavera, C. P. L. Berry, V. Kalogera, T. Fragos, P. Marchant, C. L. Rodriguez, F. Antonini, D. E. Holz, and C. Pankow, One Channel to Rule Them All? Constraining the Origins of Binary Black Holes Using Multiple Formation Pathways, *Astrophys. J.* **910**, 152 (2021), [arXiv:2011.10057 \[astro-ph.HE\]](#).
- [9] K. Belczynski, V. Kalogera, and T. Bulik, A Comprehensive study of binary compact objects as gravitational wave sources: Evolutionary channels, rates, and physical properties, *Astrophys. J.* **572**, 407 (2001), [arXiv:astro-ph/0111452](#).
- [10] M. Dominik, K. Belczynski, C. Fryer, D. E. Holz, E. Berti, T. Bulik, I. Mandel, and R. O’Shaughnessy, Double Compact Objects II: Cosmological Merger Rates, *Astrophys. J.* **779**, 72 (2013), [arXiv:1308.1546 \[astro-ph.HE\]](#).
- [11] I. Mandel and S. E. de Mink, Merging binary black holes formed through chemically homogeneous evolution in short-period stellar binaries, *Mon. Not. Roy. Astron. Soc.* **458**, 2634 (2016), [arXiv:1601.00007 \[astro-ph.HE\]](#).
- [12] K. Belczynski, D. E. Holz, T. Bulik, and R. O’Shaughnessy, The first gravitational-wave source from the isolated evolution of two 40-100 Msun stars, *Nature* **534**, 512 (2016), [arXiv:1602.04531 \[astro-ph.HE\]](#).
- [13] M. Mapelli, N. Giacobbo, E. Ripamonti, and M. Spera, The cosmic merger rate of stellar black hole binaries from the Illustris simulation, *Mon. Not. Roy. Astron. Soc.* **472**, 2422 (2017), [arXiv:1708.05722 \[astro-ph.GA\]](#).
- [14] N. Giacobbo, M. Mapelli, and M. Spera, Merging black hole binaries: the effects of progenitor’s metallicity, mass-loss rate and Eddington factor, *Mon. Not. Roy. Astron. Soc.* **474**, 2959 (2018), [arXiv:1711.03556 \[astro-ph.SR\]](#).
- [15] P. C. Peters and J. Mathews, Gravitational radiation from point masses in a Keplerian orbit, *Phys. Rev.* **131**, 435 (1963).
- [16] P. C. Peters, Gravitational Radiation and the Motion of Two Point Masses, *Phys. Rev.* **136**, B1224 (1964).
- [17] S. Naoz, The eccentric kozai-lidov effect and its applications, *Annual Review of Astronomy and Astrophysics* **54**, 441–489 (2016).
- [18] J. Samsing, Eccentric Black Hole Mergers Forming in Globular Clusters, *Phys. Rev.* **D97**, 103014 (2018), [arXiv:1711.07452 \[astro-ph.HE\]](#).
- [19] M. Zevin, J. Samsing, C. Rodriguez, C.-J. Haster, and E. Ramirez-Ruiz, Eccentric Black Hole Mergers in Dense Star Clusters: The Role of Binary–Binary Encounters, *Astrophys. J.* **871**, 91 (2019), [arXiv:1810.00901 \[astro-ph.HE\]](#).
- [20] H. Tagawa, B. Kocsis, Z. Haiman, I. Bartos, K. Omukai, and J. Samsing, Eccentric Black Hole Mergers in Active Galactic Nuclei, *Astrophys. J. Lett.* **907**, L20 (2021), [arXiv:2010.10526 \[astro-ph.HE\]](#).
- [21] I. M. Romero-Shaw, P. D. Lasky, and E. Thrane, Four Eccentric Mergers Increase the Evidence that LIGO–Virgo–KAGRA’s Binary Black Holes Form Dynamically, *Astrophys. J.* **940**, 171 (2022), [arXiv:2206.14695 \[astro-ph.HE\]](#).
- [22] M. Zevin, I. M. Romero-Shaw, K. Kremer, E. Thrane, and P. D. Lasky, Implications of Eccentric Observations on Binary Black Hole Formation Channels, *Astrophys. J. Lett.* **921**, L43 (2021), [arXiv:2106.09042 \[astro-ph.HE\]](#).
- [23] T. A. Apostolatos, C. Cutler, G. J. Sussman, and K. S. Thorne, Spin induced orbital precession and its modulation of the gravitational wave forms from merging binaries, *Phys. Rev.* **D49**, 6274 (1994).
- [24] L. E. Kidder, Coalescing binary systems of compact objects to postNewtonian 5/2 order. 5. Spin effects, *Phys. Rev.* **D52**, 821 (1995), [arXiv:gr-qc/9506022 \[gr-qc\]](#).
- [25] P. Schmidt, M. Hannam, and S. Husa, Towards models of gravitational waveforms from generic binaries: A simple approximate mapping between precessing and non-precessing inspiral signals, *Phys. Rev.* **D86**, 104063 (2012), [arXiv:1207.3088 \[gr-qc\]](#).
- [26] D. Gerosa, M. Kesden, E. Berti, R. O’Shaughnessy, and U. Sperhake, Resonant-plane locking and spin alignment in stellar-mass black-hole binaries: a diagnostic of compact-binary formation, *Phys. Rev. D* **87**, 104028 (2013), [arXiv:1302.4442 \[gr-qc\]](#).
- [27] D. Gerosa, E. Berti, R. O’Shaughnessy, K. Belczynski, M. Kesden, D. Wysocki, and W. Gladysz, Spin orientations of merging black holes formed from the evolution of stellar binaries, *Phys. Rev. D* **98**, 084036 (2018), [arXiv:1808.02491 \[astro-ph.HE\]](#).
- [28] N. Steinle and M. Kesden, Pathways for producing binary black holes with large misaligned spins in the isolated formation channel, *Phys. Rev. D* **103**, 063032 (2021), [arXiv:2010.00078 \[astro-ph.HE\]](#).
- [29] M. E. Lower, E. Thrane, P. D. Lasky, and R. Smith, Measuring eccentricity in binary black hole inspirals with gravitational waves, *Phys. Rev. D* **98**, 083028 (2018), [arXiv:1806.05350 \[astro-ph.HE\]](#).
- [30] D. Reitze *et al.*, Cosmic Explorer: The U.S. Contribu-

- tion to Gravitational-Wave Astronomy beyond LIGO, *Bull. Am. Astron. Soc.* **51**, 035 (2019), [arXiv:1907.04833 \[astro-ph.IM\]](#).
- [31] M. Maggiore *et al.*, Science Case for the Einstein Telescope, *JCAP* **03**, 050, [arXiv:1912.02622 \[astro-ph.CO\]](#).
- [32] A. K. Lenon, D. A. Brown, and A. H. Nitz, Eccentric binary neutron star search prospects for Cosmic Explorer, *Phys. Rev. D* **104**, 063011 (2021), [arXiv:2103.14088 \[astro-ph.HE\]](#).
- [33] P. Saini, Resolving the eccentricity of stellar mass binary black holes with next generation gravitational wave detectors, (2023), [arXiv:2308.07565 \[astro-ph.HE\]](#).
- [34] K. Breivik, C. L. Rodriguez, S. L. Larson, V. Kalogera, and F. A. Rasio, Distinguishing Between Formation Channels for Binary Black Holes with LISA, *Astrophys. J. Lett.* **830**, L18 (2016), [arXiv:1606.09558 \[astro-ph.GA\]](#).
- [35] A. Nishizawa, A. Sesana, E. Berti, and A. Klein, Constraining stellar binary black hole formation scenarios with eLISA eccentricity measurements, *Mon. Not. Roy. Astron. Soc.* **465**, 4375 (2017), [arXiv:1606.09295 \[astro-ph.HE\]](#).
- [36] A. Klein *et al.*, The last three years: multiband gravitational-wave observations of stellar-mass binary black holes, (2022), [arXiv:2204.03423 \[astro-ph.HE\]](#).
- [37] D. Gerosa, S. Ma, K. W. K. Wong, E. Berti, R. O’Shaughnessy, Y. Chen, and K. Belczynski, Multi-band gravitational-wave event rates and stellar physics, *Phys. Rev. D* **99**, 103004 (2019), [arXiv:1902.00021 \[astro-ph.HE\]](#).
- [38] B. Ewing, S. Sachdev, S. Borhanian, and B. S. Sathyaprakash, Archival searches for stellar-mass binary black holes in LISA data, *Phys. Rev. D* **103**, 023025 (2021), [arXiv:2011.03036 \[gr-qc\]](#).
- [39] L. Blanchet, Gravitational Radiation from Post-Newtonian Sources and Inspiralling Compact Binaries, *Living Rev. Relativity* **17**, 2 (2014), [arXiv:1310.1528 \[gr-qc\]](#).
- [40] T. Damour and N. Deruelle, General relativistic celestial mechanics of binary systems. I. The post-newtonian motion, *Annales de l’I.H.P. Physique théorique* **43**, 107 (1985).
- [41] C. W. Lincoln and C. M. Will, Coalescing binary systems of compact objects to (post)^{5/2}-newtonian order: Late-time evolution and gravitational-radiation emission, *Phys. Rev. D* **42**, 1123 (1990).
- [42] T. Damour, A. Gopakumar, and B. R. Iyer, Phasing of gravitational waves from inspiralling eccentric binaries, *Phys. Rev. D* **70**, 064028 (2004), [arXiv:gr-qc/0404128 \[gr-qc\]](#).
- [43] R.-M. Memmesheimer, A. Gopakumar, and G. Schafer, Third post-Newtonian accurate generalized quasi-Keplerian parametrization for compact binaries in eccentric orbits, *Phys. Rev. D* **70**, 104011 (2004), [arXiv:gr-qc/0407049](#).
- [44] C. Konigsdorffer and A. Gopakumar, Phasing of gravitational waves from inspiralling eccentric binaries at the third-and-a-half post-Newtonian order, *Phys. Rev. D* **73**, 124012 (2006), [arXiv:gr-qc/0603056](#).
- [45] T. Damour, P. Jaranowski, and G. Schäfer, Conservative dynamics of two-body systems at the fourth post-Newtonian approximation of general relativity, *Phys. Rev. D* **93**, 084014 (2016), [arXiv:1601.01283 \[gr-qc\]](#).
- [46] D. Bini, T. Damour, and A. Geralico, Novel approach to binary dynamics: application to the fifth post-Newtonian level, *Phys. Rev. Lett.* **123**, 231104 (2019), [arXiv:1909.02375 \[gr-qc\]](#).
- [47] D. Bini, T. Damour, and A. Geralico, Binary dynamics at the fifth and fifth-and-a-half post-Newtonian orders, *Phys. Rev. D* **102**, 024062 (2020), [arXiv:2003.11891 \[gr-qc\]](#).
- [48] J. Blümlein, A. Maier, P. Marquard, and G. Schäfer, The fifth-order post-Newtonian Hamiltonian dynamics of two-body systems from an effective field theory approach, *Nucl. Phys. B* **983**, 115900 (2022), [Erratum: *Nucl.Phys.B* 985, 115991 (2022)], [arXiv:2110.13822 \[gr-qc\]](#).
- [49] C. Dlapa, G. Kälin, Z. Liu, and R. A. Porto, Conservative Dynamics of Binary Systems at Fourth Post-Minkowskian Order in the Large-Eccentricity Expansion, *Phys. Rev. Lett.* **128**, 161104 (2022), [arXiv:2112.11296 \[hep-th\]](#).
- [50] Q. Henry and F. Larrouturou, Conservative tail and failed-tail effects at the fifth post-Newtonian order, *Phys. Rev. D* **108**, 084048 (2023), [arXiv:2307.05860 \[gr-qc\]](#).
- [51] K. G. Arun, L. Blanchet, B. R. Iyer, and M. S. S. Qusailah, Tail effects in the 3PN gravitational wave energy flux of compact binaries in quasi-elliptical orbits, *Phys. Rev. D* **77**, 064034 (2008), [arXiv:0711.0250 \[gr-qc\]](#).
- [52] K. G. Arun, L. Blanchet, B. R. Iyer, and M. S. S. Qusailah, Inspiralling compact binaries in quasi-elliptical orbits: The Complete 3PN energy flux, *Phys. Rev. D* **77**, 064035 (2008), [arXiv:0711.0302 \[gr-qc\]](#).
- [53] K. G. Arun, L. Blanchet, B. R. Iyer, and S. Sinha, Third post-Newtonian angular momentum flux and the secular evolution of orbital elements for inspiralling compact binaries in quasi-elliptical orbits, *Phys. Rev. D* **80**, 124018 (2009), [arXiv:0908.3854 \[gr-qc\]](#).
- [54] C. K. Mishra, K. G. Arun, and B. R. Iyer, Third post-Newtonian gravitational waveforms for compact binary systems in general orbits: Instantaneous terms, *Phys. Rev. D* **91**, 084040 (2015), [arXiv:1501.07096 \[gr-qc\]](#).
- [55] N. Loutrel and N. Yunes, Hereditary Effects in Eccentric Compact Binary Inspirals to Third Post-Newtonian Order, *Class. Quant. Grav.* **34**, 044003 (2017), [arXiv:1607.05409 \[gr-qc\]](#).
- [56] Y. Boetzel, C. K. Mishra, G. Faye, A. Gopakumar, and B. R. Iyer, Gravitational-wave amplitudes for compact binaries in eccentric orbits at the third post-Newtonian order: Tail contributions and postadiabatic corrections, *Phys. Rev. D* **100**, 044018 (2019), [arXiv:1904.11814 \[gr-qc\]](#).
- [57] M. Ebersold, Y. Boetzel, G. Faye, C. K. Mishra, B. R. Iyer, and P. Jetzer, Gravitational-wave amplitudes for compact binaries in eccentric orbits at the third post-Newtonian order: Memory contributions, *Phys. Rev. D* **100**, 084043 (2019), [arXiv:1906.06263 \[gr-qc\]](#).
- [58] M. Khalil, A. Buonanno, J. Steinhoff, and J. Vines, Radiation-reaction force and multipolar waveforms for eccentric, spin-aligned binaries in the effective-one-body formalism, *Phys. Rev. D* **104**, 024046 (2021), [arXiv:2104.11705 \[gr-qc\]](#).
- [59] K. Paul and C. K. Mishra, Spin effects in spherical harmonic modes of gravitational waves from eccentric compact binary inspirals, *Phys. Rev. D* **108**, 024023 (2023), [arXiv:2211.04155 \[gr-qc\]](#).

- [60] N. Yunes, K. G. Arun, E. Berti, and C. M. Will, Post-Circular Expansion of Eccentric Binary Inspirals: Fourier-Domain Waveforms in the Stationary Phase Approximation, *Phys. Rev. D* **80**, 084001 (2009), [Erratum: *Phys. Rev. D* **89**, 109901 (2014)], [arXiv:0906.0313 \[gr-qc\]](#).
- [61] M. Tessmer and G. Schaefer, Full-analytic frequency-domain 1pN-accurate gravitational wave forms from eccentric compact binaries, *Phys. Rev. D* **82**, 124064 (2010), [arXiv:1006.3714 \[gr-qc\]](#).
- [62] S. Tanay, M. Haney, and A. Gopakumar, Frequency and time domain inspiral templates for comparable mass compact binaries in eccentric orbits, *Phys. Rev. D* **93**, 064031 (2016), [arXiv:1602.03081 \[gr-qc\]](#).
- [63] A. Klein, Y. Boetzel, A. Gopakumar, P. Jetzer, and L. de Vittori, Fourier domain gravitational waveforms for precessing eccentric binaries, *Phys. Rev. D* **98**, 104043 (2018), [arXiv:1801.08542 \[gr-qc\]](#).
- [64] B. Moore and N. Yunes, A 3PN Fourier Domain Waveform for Non-Spinning Binaries with Moderate Eccentricity, *Class. Quant. Grav.* **36**, 185003 (2019), [arXiv:1903.05203 \[gr-qc\]](#).
- [65] S. Tiwari and A. Gopakumar, Combining post-circular and Padé approximations to compute Fourier domain templates for eccentric inspirals, *Phys. Rev. D* **102**, 084042 (2020), [arXiv:2009.11333 \[gr-qc\]](#).
- [66] S. Hopper, C. Kavanagh, and A. C. Ottewill, Analytic self-force calculations in the post-Newtonian regime: eccentric orbits on a Schwarzschild background, *Phys. Rev. D* **93**, 044010 (2016), [arXiv:1512.01556 \[gr-qc\]](#).
- [67] E. Forseth, C. R. Evans, and S. Hopper, Eccentric-orbit extreme-mass-ratio inspiral gravitational wave energy fluxes to 7PN order, *Phys. Rev. D* **93**, 064058 (2016), [arXiv:1512.03051 \[gr-qc\]](#).
- [68] D. Bini and T. Damour, Gravitational scattering of two black holes at the fourth post-Newtonian approximation, *Phys. Rev. D* **96**, 064021 (2017), [arXiv:1706.06877 \[gr-qc\]](#).
- [69] C. Kavanagh, D. Bini, T. Damour, S. Hopper, A. C. Ottewill, and B. Wardell, Spin-orbit precession along eccentric orbits for extreme mass ratio black hole binaries and its effective-one-body transcription, *Phys. Rev. D* **96**, 064012 (2017), [arXiv:1706.00459 \[gr-qc\]](#).
- [70] C. Munna, Analytic post-Newtonian expansion of the energy and angular momentum radiated to infinity by eccentric-orbit nonspinning extreme-mass-ratio inspirals to the 19th order, *Phys. Rev. D* **102**, 124001 (2020), [arXiv:2008.10622 \[gr-qc\]](#).
- [71] P. Lynch, M. van de Meent, and N. Warburton, Eccentric self-forced inspirals into a rotating black hole, *Class. Quant. Grav.* **39**, 145004 (2022), [arXiv:2112.05651 \[gr-qc\]](#).
- [72] A. Albertini, R. Gamba, A. Nagar, and S. Bernuzzi, Effective-one-body waveforms for extreme-mass-ratio binaries: Consistency with second-order gravitational self-force quasicircular results and extension to non-precessing spins and eccentricity, *Phys. Rev. D* **109**, 044022 (2024), [arXiv:2310.13578 \[gr-qc\]](#).
- [73] A. Ramos-Buades, S. Husa, G. Pratten, H. Estellés, C. García-Quirós, M. Mateu-Lucena, M. Colleoni, and R. Jaume, First survey of spinning eccentric black hole mergers: Numerical relativity simulations, hybrid waveforms, and parameter estimation, *Phys. Rev. D* **101**, 083015 (2020), [arXiv:1909.11011 \[gr-qc\]](#).
- [74] U. Sperhake, R. Rosca-Mead, D. Gerosa, and E. Berti, Amplification of superkicks in black-hole binaries through orbital eccentricity, *Phys. Rev. D* **101**, 024044 (2020), [arXiv:1910.01598 \[gr-qc\]](#).
- [75] A. Ramos-Buades, M. van de Meent, H. P. Pfeiffer, H. R. Rüter, M. A. Scheel, M. Boyle, and L. E. Kidder, Eccentric binary black holes: Comparing numerical relativity and small mass-ratio perturbation theory, *Phys. Rev. D* **106**, 124040 (2022), [arXiv:2209.03390 \[gr-qc\]](#).
- [76] J. Healy and C. O. Lousto, Fourth RIT binary black hole simulations catalog: Extension to eccentric orbits, *Phys. Rev. D* **105**, 124010 (2022), [arXiv:2202.00018 \[gr-qc\]](#).
- [77] A. V. Joshi, S. G. Rosofsky, R. Haas, and E. A. Huerta, Numerical relativity higher order gravitational waveforms of eccentric, spinning, nonprecessing binary black hole mergers, *Phys. Rev. D* **107**, 064038 (2023), [arXiv:2210.01852 \[gr-qc\]](#).
- [78] D. Ferguson *et al.*, Second MAYA Catalog of Binary Black Hole Numerical Relativity Waveforms, (2023), [arXiv:2309.00262 \[gr-qc\]](#).
- [79] T. Islam, V. Varma, J. Lodman, S. E. Field, G. Khanna, M. A. Scheel, H. P. Pfeiffer, D. Gerosa, and L. E. Kidder, Eccentric binary black hole surrogate models for the gravitational waveform and remnant properties: comparable mass, nonspinning case, *Phys. Rev. D* **103**, 064022 (2021), [arXiv:2101.11798 \[gr-qc\]](#).
- [80] E. A. Huerta *et al.*, Eccentric, nonspinning, inspiral, Gaussian-process merger approximant for the detection and characterization of eccentric binary black hole mergers, *Phys. Rev. D* **97**, 024031 (2018), [arXiv:1711.06276 \[gr-qc\]](#).
- [81] I. Hinder, L. E. Kidder, and H. P. Pfeiffer, Eccentric binary black hole inspiral-merger-ringdown gravitational waveform model from numerical relativity and post-Newtonian theory, *Phys. Rev. D* **98**, 044015 (2018), [arXiv:1709.02007 \[gr-qc\]](#).
- [82] G. Cho, S. Tanay, A. Gopakumar, and H. M. Lee, Generalized quasi-Keplerian solution for eccentric, nonspinning compact binaries at 4PN order and the associated inspiral-merger-ringdown waveform, *Phys. Rev. D* **105**, 064010 (2022), [arXiv:2110.09608 \[gr-qc\]](#).
- [83] A. Chattaraj, T. RoyChowdhury, Divyajyoti, C. K. Mishra, and A. Gupta, High accuracy post-Newtonian and numerical relativity comparisons involving higher modes for eccentric binary black holes and a dominant mode eccentric inspiral-merger-ringdown model, *Phys. Rev. D* **106**, 124008 (2022), [arXiv:2204.02377 \[gr-qc\]](#).
- [84] A. Buonanno and T. Damour, Effective one-body approach to general relativistic two-body dynamics, *Phys. Rev. D* **59**, 084006 (1999), [arXiv:gr-qc/9811091](#).
- [85] A. Buonanno and T. Damour, Transition from inspiral to plunge in binary black hole coalescences, *Phys. Rev. D* **62**, 064015 (2000), [arXiv:gr-qc/0001013](#).
- [86] T. Damour, P. Jaranowski, and G. Schaefer, On the determination of the last stable orbit for circular general relativistic binaries at the third postNewtonian approximation, *Phys. Rev. D* **62**, 084011 (2000), [arXiv:gr-qc/0005034 \[gr-qc\]](#).
- [87] T. Damour, Coalescence of two spinning black holes: An effective one-body approach, *Phys. Rev. D* **64**, 124013 (2001), [arXiv:gr-qc/0103018](#).
- [88] D. Bini and T. Damour, Gravitational radiation reaction along general orbits in the effective one-body formalism, *Phys. Rev. D* **86**, 124012 (2012),

- arXiv:1210.2834 [gr-qc].
- [89] T. Hinderer and S. Babak, Foundations of an effective one-body model for coalescing binaries on eccentric orbits, *Phys. Rev. D* **D96**, 104048 (2017), arXiv:1707.08426 [gr-qc].
- [90] Z. Cao and W.-B. Han, Waveform model for an eccentric binary black hole based on the effective-one-body-numerical-relativity formalism, *Phys. Rev. D* **D96**, 044028 (2017), arXiv:1708.00166 [gr-qc].
- [91] X. Liu, Z. Cao, and L. Shao, Validating the Effective-One-Body Numerical-Relativity Waveform Models for Spin-aligned Binary Black Holes along Eccentric Orbits, *Phys. Rev. D* **101**, 044049 (2020), arXiv:1910.00784 [gr-qc].
- [92] D. Chiamello and A. Nagar, Faithful analytical effective-one-body waveform model for spin-aligned, moderately eccentric, coalescing black hole binaries, *Phys. Rev. D* **101**, 101501 (2020), arXiv:2001.11736 [gr-qc].
- [93] A. Nagar, A. Bonino, and P. Retegno, Effective one-body multipolar waveform model for spin-aligned, quasi-circular, eccentric, hyperbolic black hole binaries, *Phys. Rev. D* **103**, 104021 (2021), arXiv:2101.08624 [gr-qc].
- [94] A. Placidi, S. Albanesi, A. Nagar, M. Orselli, S. Bernuzzi, and G. Grignani, Exploiting Newton-factorized, 2PN-accurate waveform multipoles in effective-one-body models for spin-aligned noncircularized binaries, *Phys. Rev. D* **105**, 104030 (2022), arXiv:2112.05448 [gr-qc].
- [95] A. Albertini, A. Nagar, P. Retegno, S. Albanesi, and R. Gamba, Waveforms and fluxes: Towards a self-consistent effective one body waveform model for non-precessing, coalescing black-hole binaries for third generation detectors, *Phys. Rev. D* **105**, 084025 (2022), arXiv:2111.14149 [gr-qc].
- [96] S. Albanesi, A. Nagar, S. Bernuzzi, A. Placidi, and M. Orselli, Assessment of effective-one-body radiation reactions for generic planar orbits, *Phys. Rev. D* **105**, 104031 (2022), arXiv:2202.10063 [gr-qc].
- [97] S. Albanesi, A. Placidi, A. Nagar, M. Orselli, and S. Bernuzzi, New avenue for accurate analytical waveforms and fluxes for eccentric compact binaries, *Phys. Rev. D* **105**, L121503 (2022), arXiv:2203.16286 [gr-qc].
- [98] A. Ramos-Buades, A. Buonanno, M. Khalil, and S. Ossokine, Effective-one-body multipolar waveforms for eccentric binary black holes with nonprecessing spins, *Phys. Rev. D* **105**, 044035 (2022), arXiv:2112.06952 [gr-qc].
- [99] X. Liu, Z. Cao, and Z.-H. Zhu, A higher-multipole gravitational waveform model for an eccentric binary black holes based on the effective-one-body-numerical-relativity formalism, *Class. Quant. Grav.* **39**, 035009 (2022), arXiv:2102.08614 [gr-qc].
- [100] Q. Yun, W.-B. Han, X. Zhong, and C. A. Benavides-Gallego, Surrogate model for gravitational waveforms of spin-aligned binary black holes with eccentricities, *Phys. Rev. D* **103**, 124053 (2021), arXiv:2104.03789 [gr-qc].
- [101] Q. Henry and M. Khalil, Spin effects in gravitational waveforms and fluxes for binaries on eccentric orbits to the third post-Newtonian order, *Phys. Rev. D* **108**, 104016 (2023), arXiv:2308.13606 [gr-qc].
- [102] X. Liu, Z. Cao, and L. Shao, Upgraded waveform model of eccentric binary black hole based on effective-one-body-numerical-relativity for spin-aligned binary black holes, *Int. J. Mod. Phys. D* **32**, 2350015 (2023), arXiv:2306.15277 [gr-qc].
- [103] A. Nagar and P. Retegno, Next generation: Impact of high-order analytical information on effective one body waveform models for noncircularized, spin-aligned black hole binaries, *Phys. Rev. D* **104**, 104004 (2021), arXiv:2108.02043 [gr-qc].
- [104] S. Albanesi, A. Nagar, and S. Bernuzzi, Effective one-body model for extreme-mass-ratio spinning binaries on eccentric equatorial orbits: Testing radiation reaction and waveform, *Phys. Rev. D* **104**, 024067 (2021), arXiv:2104.10559 [gr-qc].
- [105] A. Nagar, P. Retegno, R. Gamba, and S. Bernuzzi, Effective-one-body waveforms from dynamical captures in black hole binaries, *Phys. Rev. D* **103**, 064013 (2021), arXiv:2009.12857 [gr-qc].
- [106] X. Liu, Z. Cao, and Z.-H. Zhu, Effective-One-Body Numerical-Relativity waveform model for Eccentric spin-precessing binary black hole coalescence, (2023), arXiv:2310.04552 [gr-qc].
- [107] A. Vijaykumar, A. G. Hanselman, and M. Zevin, Consistent eccentricities for gravitational wave astronomy: Resolving discrepancies between astrophysical simulations and waveform models, (2024), arXiv:2402.07892 [astro-ph.HE].
- [108] A. Bonino, R. Gamba, P. Schmidt, A. Nagar, G. Pratten, M. Breschi, P. Retegno, and S. Bernuzzi, Inferring eccentricity evolution from observations of coalescing binary black holes, *Phys. Rev. D* **107**, 064024 (2023), arXiv:2207.10474 [gr-qc].
- [109] F. Loffler *et al.*, The Einstein Toolkit: A Community Computational Infrastructure for Relativistic Astrophysics, *Class. Quant. Grav.* **29**, 115001 (2012), arXiv:1111.3344 [gr-qc].
- [110] S. R. Brand *et al.*, *The einstein toolkit* (2021).
- [111] M. Campanelli, C. O. Lousto, P. Marronetti, and Y. Zlochower, Accurate Evolutions of Orbiting Black-Hole Binaries Without Excision, *Phys. Rev. Lett.* **96**, 111101 (2006), arXiv:gr-qc/0511048.
- [112] J. G. Baker, J. Centrella, D.-I. Choi, M. Koppitz, and J. van Meter, Gravitational wave extraction from an inspiraling configuration of merging black holes, *Phys. Rev. Lett.* **96**, 111102 (2006), arXiv:gr-qc/0511103.
- [113] J. M. Bowen and J. W. York, Jr., Time asymmetric initial data for black holes and black hole collisions, *Phys. Rev. D* **D21**, 2047 (1980).
- [114] S. Brandt and B. Brügmann, A Simple construction of initial data for multiple black holes, *Phys. Rev. Lett.* **78**, 3606 (1997), arXiv:gr-qc/9703066.
- [115] M. Ansorg, B. Brügmann, and W. Tichy, A single-domain spectral method for black hole puncture data, *Phys. Rev. D* **D70**, 064011 (2004), arXiv:gr-qc/0404056.
- [116] P. Marronetti, W. Tichy, B. Brügmann, J. Gonzalez, and U. Sperhake, High-spin binary black hole mergers, *Phys. Rev. D* **D77**, 064010 (2008), arXiv:0709.2160 [gr-qc].
- [117] M. Shibata and T. Nakamura, Evolution of three-dimensional gravitational waves: Harmonic slicing case, *Phys. Rev. D* **D52**, 5428 (1995).
- [118] T. W. Baumgarte and S. L. Shapiro, On the numerical integration of Einstein's field equations, *Phys. Rev. D* **D59**, 024007 (1999), arXiv:gr-qc/9810065.
- [119] C. Bona, J. Massó, E. Seidel, and J. Stela, New Formalism for Numerical Relativity, *Phys. Rev. Lett.* **75**, 600

- (1995), [gr-qc/9412071](#).
- [120] M. Alcubierre, B. Brügmann, P. Diener, M. Koppitz, D. Pollney, *et al.*, Gauge conditions for long term numerical black hole evolutions without excision, *Phys.Rev.* **D67**, 084023 (2003), [arXiv:gr-qc/0206072 \[gr-qc\]](#).
- [121] H. O. Kreiss and J. Oliger, *Methods for the approximate solution of time dependent problems* (International Council of Scientific Unions, World Meteorological Organization, Geneva, 1973).
- [122] J. Thornburg, Black hole excision with multiple grid patches, *Class.Quant.Grav.* **21**, 3665 (2004), [arXiv:gr-qc/0404059 \[gr-qc\]](#).
- [123] A. Ashtekar and B. Krishnan, Dynamical horizons and their properties, *Phys. Rev. D* **68**, 104030 (2003), [arXiv:gr-qc/0308033](#).
- [124] O. Dreyer, B. J. Kelly, B. Krishnan, L. S. Finn, D. Garrison, and R. Lopez-Aleman, Black hole spectroscopy: Testing general relativity through gravitational wave observations, *Class. Quant. Grav.* **21**, 787 (2004), [arXiv:gr-qc/0309007 \[gr-qc\]](#).
- [125] E. Schnetter, B. Krishnan, and F. Beyer, Introduction to dynamical horizons in numerical relativity, *Phys. Rev. D* **74**, 024028 (2006), [arXiv:gr-qc/0604015](#).
- [126] E. Schnetter, S. H. Hawley, and I. Hawke, Evolutions in 3-D numerical relativity using fixed mesh refinement, *Class.Quant.Grav.* **21**, 1465 (2004), [arXiv:gr-qc/0310042 \[gr-qc\]](#).
- [127] D. Pollney, C. Reisswig, E. Schnetter, N. Dorband, and P. Diener, High accuracy binary black hole simulations with an extended wave zone, *Phys. Rev.* **D83**, 044045 (2011), [arXiv:0910.3803 \[gr-qc\]](#).
- [128] C. Reisswig, R. Haas, C. D. Ott, E. Abdikamalov, P. Mösta, D. Pollney, and E. Schnetter, Three-Dimensional General-Relativistic Hydrodynamic Simulations of Binary Neutron Star Coalescence and Stellar Collapse with Multipatch Grids, *Phys. Rev.* **D87**, 064023 (2013), [arXiv:1212.1191 \[astro-ph.HE\]](#).
- [129] E. Newman and R. Penrose, An Approach to gravitational radiation by a method of spin coefficients, *J. Math. Phys.* **3**, 566 (1962).
- [130] C. Reisswig and D. Pollney, Notes on the integration of numerical relativity waveforms, *Class.Quant.Grav.* **28**, 195015 (2011), [arXiv:1006.1632 \[gr-qc\]](#).
- [131] M. Boyle and A. H. Mroue, Extrapolating gravitational-wave data from numerical simulations, *Phys. Rev.* **D80**, 124045 (2009), [arXiv:0905.3177 \[gr-qc\]](#).
- [132] I. Hinder, A. Buonanno, M. Boyle, Z. B. Etienne, J. Healy, *et al.*, Error-analysis and comparison to analytical models of numerical waveforms produced by the NRAR Collaboration, *Class.Quant.Grav.* **31**, 025012 (2013), [arXiv:1307.5307 \[gr-qc\]](#).
- [133] H. Nakano, J. Healy, C. O. Lousto, and Y. Zlochower, Perturbative extraction of gravitational waveforms generated with Numerical Relativity, *Phys. Rev. D* **91**, 104022 (2015), [arXiv:1503.00718 \[gr-qc\]](#).
- [134] A. Ramos-Buades, S. Husa, and G. Pratten, Simple procedures to reduce eccentricity of binary black hole simulations, *Phys. Rev. D* **99**, 023003 (2019), [arXiv:1810.00036 \[gr-qc\]](#).
- [135] D. Christodoulou, Reversible and irreversible transformations in black hole physics, *Phys. Rev. Lett.* **25**, 1596 (1970).
- [136] X. Jiménez-Forteza, D. Keitel, S. Husa, M. Hannam, S. Khan, and M. Pürrer, Hierarchical data-driven approach to fitting numerical relativity data for non-precessing binary black holes with an application to final spin and radiated energy, *Phys. Rev.* **D95**, 064024 (2017), [arXiv:1611.00332 \[gr-qc\]](#).
- [137] M. Ruiz, R. Takahashi, M. Alcubierre, and D. Nunez, Multipole expansions for energy and momenta carried by gravitational waves, *Gen. Rel. Grav.* **40**, 2467 (2008), [arXiv:0707.4654 \[gr-qc\]](#).
- [138] D. Keitel *et al.*, The most powerful astrophysical events: Gravitational-wave peak luminosity of binary black holes as predicted by numerical relativity, *Phys. Rev.* **D96**, 024006 (2017), [arXiv:1612.09566 \[gr-qc\]](#).
- [139] A. H. Mroue, H. P. Pfeiffer, L. E. Kidder, and S. A. Teukolsky, Measuring orbital eccentricity and periastron advance in quasi-circular black hole simulations, *Phys. Rev. D* **82**, 124016 (2010), [arXiv:1004.4697 \[gr-qc\]](#).
- [140] T. Mora and C. M. Will, Numerically generated quasiequilibrium orbits of black holes: Circular or eccentric?, *Phys. Rev. D* **66**, 101501 (2002), [arXiv:gr-qc/0208089](#).
- [141] T. Mora and C. M. Will, A Post-Newtonian diagnostic of quasi-equilibrium binary configurations of compact objects, *Phys. Rev.* **D69**, 104021 (2004), [Erratum: *Phys. Rev.* D71, 129901 (2005)], [arXiv:gr-qc/0312082 \[gr-qc\]](#).
- [142] N. Loutrel, S. Liebersbach, N. Yunes, and N. Cornish, The eccentric behavior of inspiralling compact binaries, *Class. Quant. Grav.* **36**, 025004 (2019), [arXiv:1810.03521 \[gr-qc\]](#).
- [143] M. A. Shaikh, V. Varma, H. P. Pfeiffer, A. Ramos-Buades, and M. van de Meent, Defining eccentricity for gravitational wave astronomy, (2023), [arXiv:2302.11257 \[gr-qc\]](#).
- [144] A. Ramos-Buades, A. Buonanno, and J. Gair, Bayesian inference of binary black holes with inspiral-merger-ringdown waveforms using two eccentric parameters, (2023), [arXiv:2309.15528 \[gr-qc\]](#).
- [145] T. Damour and G. Schäfer, Higher Order Relativistic Periastron Advances and Binary Pulsars, *Nuovo Cim.* **B101**, 127 (1988).
- [146] G. Carullo, S. Albanesi, A. Nagar, R. Gamba, S. Bernuzzi, T. Andrade, and J. Trenado, Unveiling the Merger Structure of Black Hole Binaries in Generic Planar Orbits, *Phys. Rev. Lett.* **132**, 101401 (2024), [arXiv:2309.07228 \[gr-qc\]](#).
- [147] R. Gamba, M. Breschi, G. Carullo, P. Rettegno, S. Albanesi, S. Bernuzzi, and A. Nagar, GW190521: A dynamical capture of two black holes, Submitted to Nature Astronomy (2021), [arXiv:2106.05575 \[gr-qc\]](#).
- [148] M. Pürrer, S. Husa, and M. Hannam, An Efficient iterative method to reduce eccentricity in numerical-relativity simulations of compact binary inspiral, *Phys. Rev. D* **85**, 124051 (2012), [arXiv:1203.4258 \[gr-qc\]](#).
- [149] A. Ramos-Buades, P. Schmidt, G. Pratten, and S. Husa, Validity of common modeling approximations for precessing binary black holes with higher-order modes, *Phys. Rev. D* **101**, 103014 (2020), [arXiv:2001.10936 \[gr-qc\]](#).
- [150] T. Regge and J. A. Wheeler, Stability of a Schwarzschild singularity, *Phys. Rev.* **108**, 1063 (1957).
- [151] F. J. Zerilli, Effective potential for even parity Regge-Wheeler gravitational perturbation equations, *Phys. Rev. Lett.* **24**, 737 (1970).

- [152] O. Sarbach and M. Tiglio, Gauge invariant perturbations of Schwarzschild black holes in horizon-penetrating coordinates, *Phys. Rev.* **D64**, 084016 (2001), [gr-qc/0104061](#).
- [153] M. Boyle *et al.*, The SXS Collaboration catalog of binary black hole simulations, *Class. Quant. Grav.* **36**, 195006 (2019), [arXiv:1904.04831 \[gr-qc\]](#).
- [154] T. Damour and A. Nagar, New effective-one-body description of coalescing nonprecessing spinning black-hole binaries, *Phys.Rev.* **D90**, 044018 (2014), [arXiv:1406.6913 \[gr-qc\]](#).
- [155] A. Nagar, G. Pratten, G. Riemenschneider, and R. Gamba, Multipolar effective one body model for non-spinning black hole binaries, *Phys. Rev. D* **101**, 024041 (2020), [arXiv:1904.09550 \[gr-qc\]](#).
- [156] A. Nagar, G. Riemenschneider, G. Pratten, P. Rettegnò, and F. Messina, Multipolar effective one body waveform model for spin-aligned black hole binaries, *Phys. Rev. D* **102**, 024077 (2020), [arXiv:2001.09082 \[gr-qc\]](#).
- [157] G. Riemenschneider, P. Rettegnò, M. Breschi, A. Albertini, R. Gamba, S. Bernuzzi, and A. Nagar, Assessment of consistent next-to-quasicircular corrections and postadiabatic approximation in effective-one-body multipolar waveforms for binary black hole coalescences, *Phys. Rev. D* **104**, 104045 (2021), [arXiv:2104.07533 \[gr-qc\]](#).
- [158] A. M. Knee, I. M. Romero-Shaw, P. D. Lasky, J. McIver, and E. Thrane, A Rosetta Stone for Eccentric Gravitational Waveform Models, *Astrophys. J.* **936**, 172 (2022), [arXiv:2207.14346 \[gr-qc\]](#).
- [159] A. Nagar and P. Rettegnò, Efficient effective one body time-domain gravitational waveforms, *Phys. Rev.* **D99**, 021501 (2019), [arXiv:1805.03891 \[gr-qc\]](#).
- [160] B. P. Abbott *et al.* (KAGRA, LIGO Scientific, Virgo, VIRGO), Prospects for observing and localizing gravitational-wave transients with Advanced LIGO, Advanced Virgo and KAGRA, *Living Rev. Rel.* **21**, 3 (2020), [arXiv:1304.0670 \[gr-qc\]](#).
- [161] LIGO Scientific Collaboration, Virgo Collaboration, and KAGRA Collaboration, *Noise curves used for Simulations in the update of the Observing Scenarios Paper*, Tech. Rep. LIGO-T2000012-v2 (2022).
- [162] W. R. Inc., *Mathematica, Version 14.0*, Champaign, IL, 2024.
- [163] J. D. Hunter, Matplotlib: A 2d graphics environment, *Computing In Science & Engineering* **9**, 90 (2007).
- [164] S. Bernuzzi, A. Nagar, *et al.*, *TEOBResumS Bitbucket Repository* (2024).
- [165] I. Hinder, F. Herrmann, P. Laguna, and D. Shoemaker, Comparisons of eccentric binary black hole simulations with post-Newtonian models, *Phys. Rev.* **D82**, 024033 (2010), [arXiv:0806.1037 \[gr-qc\]](#).